SCIENCE CHINA
Earth Sciences

• RESEARCH PAPER •

October 2017 Vol.60 No.10: 1866–1885
doi: 10.1007/s11430-017-9076-9

Assimilating Doppler radar observations with an ensemble Kalman filter for convection-permitting prediction of convective development in a heavy rainfall event during the pre-summer rainy season of South China

BAO XingHua[1], LUO YaLi[1,2*], SUN JiaXiang[3], MENG ZhiYong[4] & YUE Jian[5]

[1] *State Key Laboratory of Severe Weather, Chinese Academy of Meteorological Sciences, Beijing 100081, China;*
[2] *Collaborative Innovation Center on Forecast and Evaluation of Meteorological Disasters, Nanjing University of Information Science and Technology, Nanjing 210044, China;*
[3] *CAAC East China Regional Air Traffic Administration, Shanghai 200335, China;*
[4] *Laboratory for Climate and Ocean-Atmosphere Studies, Department of Atmospheric and Oceanic Sciences, School of Physics, Peking University, Beijing 100871, China;*
[5] *National Meteorological Center, China Meteorological Administration, Beijing 100081, China*

Received January 3, 2017; accepted June 22, 2017; published online September 5, 2017

Abstract This study examines the effectiveness of an ensemble Kalman filter based on the weather research and forecasting model to assimilate Doppler-radar radial-velocity observations for convection-permitting prediction of convection evolution in a high-impact heavy-rainfall event over coastal areas of South China during the pre-summer rainy season. An ensemble of 40 deterministic forecast experiments (40 DADF) with data assimilation (DA) is conducted, in which the DA starts at the same time but lasts for different time spans (up to 2 h) and with different time intervals of 6, 12, 24, and 30 min. The reference experiment is conducted without DA (NODA).To show more clearly the impact of radar DA on mesoscale convective system (MCS) forecasts, two sets of 60-member ensemble experiments (NODA EF and exp37 EF) are performed using the same 60-member perturbed-ensemble initial fields but with the radar DA being conducted every 6 min in the exp37 EF experiments from 0200 to 0400 BST. It is found that the DA experiments generally improve the convection prediction. The 40 DADF experiments can forecast a heavy-rain-producing MCS over land and an MCS over the ocean with high probability, despite slight displacement errors. The exp37 EF improves the probability forecast of inland and offshore MCSs more than does NODA EF. Compared with the experiments using the longer DA time intervals, assimilating the radial-velocity observations at 6-min intervals tends to produce better forecasts. The experiment with the longest DA time span and shortest time interval shows the best performance. However, a shorter DA time interval (e.g., 12 min) or a longer DA time span does not always help. The experiment with the shortest DA time interval and maximum DA window shows the best performance, as it corrects errors in the simulated convection evolution over both the inland and offshore areas. An improved representation of the initial state leads to dynamic and thermodynamic conditions that are more conducive to earlier initiation of the inland MCS and longer maintenance of the offshore MCS.

Keywords Radial velocity, EnKF, Heavy rainfall forecast, Pre-summer rainy season, South China

Citation: Bao X H, Luo Y L, Sun J X, Meng Z Y, Yue J. 2017. Assimilating Doppler radar observations with an ensemble Kalman filter for convection-permitting prediction of convective development in a heavy rainfall event during the pre-summer rainy season of South China. Science China Earth Sciences, 60: 1866–1885, doi: 10.1007/s11430-017-9076-9

* Corresponding author (email: yali@camscma.cn)

1. Introduction

The pre-summer rainy season (April–June) of South China is the longest rainy season with the most abundant rainfall amount over China. Precipitation in this rainy season accounts for 40–50% of the annual cumulative precipitation in South China (Ding, 1992, 1994). Precipitation during the pre-summer rainy season is mostly of a convective nature with mesoscale organizational characteristics (Xu et al., 2009; Luo et al., 2013), is frequent and of strong intensity, and often causes severe flooding and inundation. The heavy-rainfall-producing mesoscale convective systems (MCSs) impact the highly populated inland areas as well as the coastal and offshore areas where human activities such as fisheries, marine transportation, and marine leisure are intense. Moreover, those MCSs often develop in prevailing low-level southwesterly flows with subtle synoptic lifting, and pose a major challenge to numerical weather prediction (NWP) for Southern China.

The Southern China Monsoon Rainfall Experiment (SCMREX; http://scmrex.cma.gov.cn) is a research and development project (RDP) of the World Meteorological Organization's World Weather Research Program (Luo et al., 2017; Luo, 2017). SCMREX aims to advance the understanding of the key processes leading to heavy rain and to expedite the efforts to improve the prediction of heavy rainfall during the pre-summer rainy season in Southern China and its vicinity. This is done via field campaigns, NWP studies (e.g., Zhang et al., 2016), and studies of physical mechanisms (e.g., Wang et al., 2014; Wu and Luo, 2016). The pilot field experiments of SCMREX were carried out over Southern China during May to mid-June of 2013–2015. Four heavy-rainfall events occurred during the intensive observing periods (IOPs) of SCMREX-2013 (8–17 and 24–28 May). The first event occurred on May 8, 2013, during which five MCSs—two mostly inland, one around the coastal line, and two offshore—were observed by the Yangjiang S-band radar (Figure 1a–j; radar location shown in Figure 1k). The accumulated rainfall reached

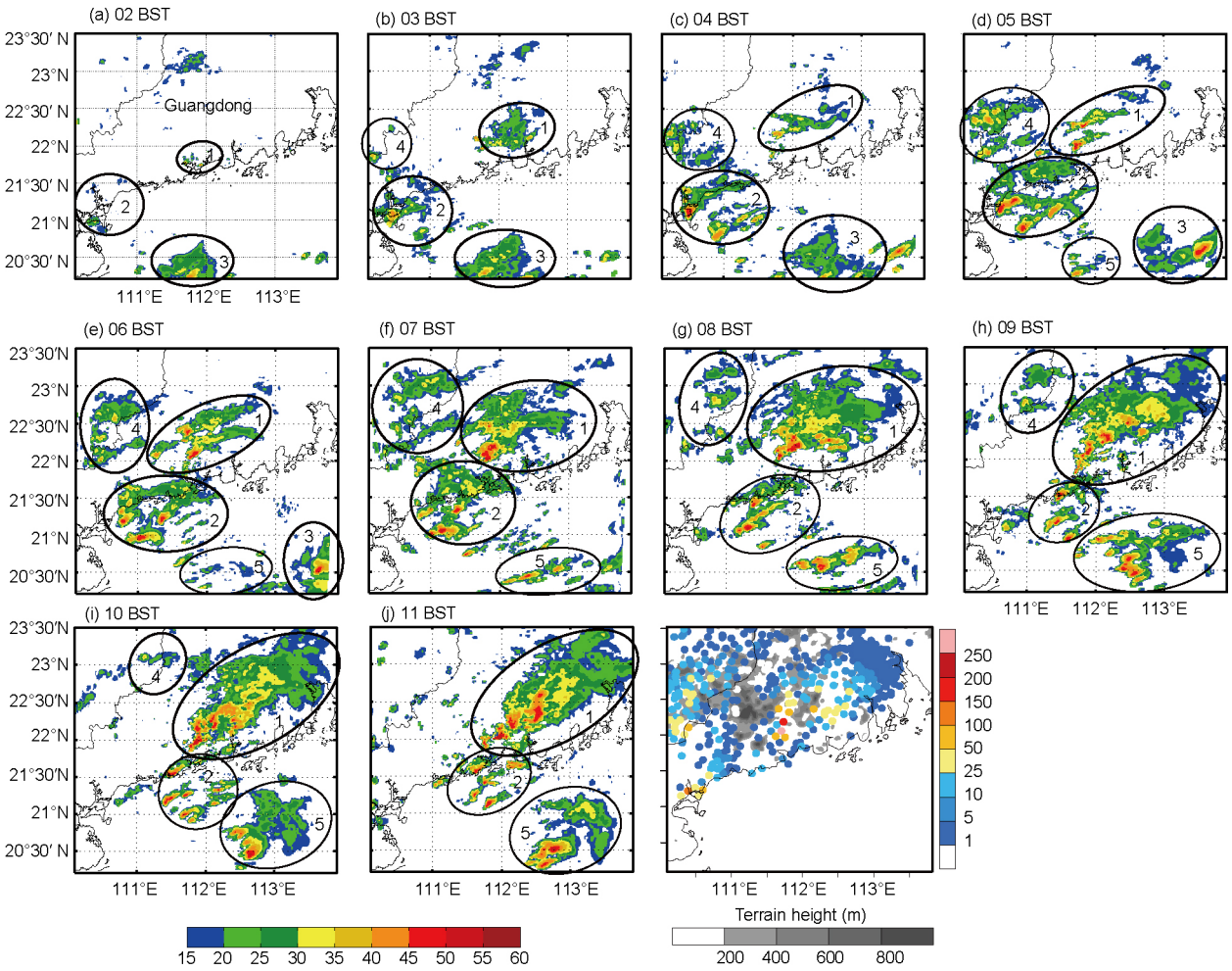

Figure 1 (a)–(j) Radar reflectivity (dBZ; color bar at the bottom) at 3 km ASL derived from the Yangjiang radar during 0200–1100 BST 8 May 2013. Each of ellipses 1–5 indicates the region of a correspondingly numbered MCS. (k) Accumulated rainfall during 0400–1100 BST 8 May 2013 based on rain-gauge observations (color bar to the right). The gray shading and the red cross in (k) represent topography and the location of the Yangjiang radar, respectively. The gray lines in each panel represent coastlines and provincial boundaries.

a maximum of 285 mm, causing severe flooding and huge economic losses. However, this heavy-rainfall event was missed by the operational forecast at the National Meteorological Center of China. The present work examines the effectiveness of assimilating the Yangjiang-radar radial-velocity observations with an ensemble Kalman filter (EnKF) on the prediction of these MCSs and the associated heavy precipitation.

The EnKF data assimilation (DA) technique uses an ensemble of short-term forecasts to estimate the flow-dependent background error covariance (Evensen, 1994). Focusing on tropical cyclone (TC) prediction, a number of studies have utilized the EnKF method to assimilate ground-based-radar radial velocity (Zhang et al., 2009; Zhu et al., 2016; Yue and Meng, 2017; Yue et al., 2017), ground-based-radar reflectivity and radial velocity (Xue and Dong, 2013; Dong and Xue, 2013), and airborne-radar radial velocity (Weng and Zhang, 2012; Zhang and Weng, 2015). Because of the DA, those studies found remarkable improvement in the forecasts of TC vortex initialization, intensity, track, and precipitation, as well as the analysis of TC structure. Moreover, some studies have demonstrated significant improvements in forecasting the evolution of tornadic MCSs over the United States (Snook et al., 2011, 2012, 2015) and the location of MCS-produced extreme precipitation over central East China (Qiu and Zhang, 2016) by assimilating radar observations using the EnKF technique.

Although there is a dearth of conventional observations over the oceans, Doppler weather radars in coastal areas can scan parts of the offshore areas and offer complete spatial and temporal coverage of kinematic fields. Such coastal radars can therefore potentially improve NWP performance through successful DA. A few studies have assimilated coastal-radar data with EnKFs to explore the impact of the latter on the prediction of TCs impacting China (e.g., Zhu et al., 2016). However, the literature still contains relatively few studies on the influence of radar DA on the forecast of heavy-rain-producing MCSs over Southern China. Moreover, the time intervals of radar DA differ among previous studies. For example, the time interval varies from 10 min (Xue and Dong, 2013; Dong and Xue, 2013) to 1 h (Zhang et al., 2009) in the TC studies, and from 5 min (Snook et al., 2011, 2012, 2015) to 1 h (Qiu and Zhang, 2016) in the MCS studies. The time interval also varied during the DA period in a TC case study (Weng and Zhang, 2012). However, the influence of different DA time intervals on MCS prediction is unknown.

The present study has two objectives. One is to show the potential benefit of the EnKF technique assimilated with radar radial velocity from operational weather radars in coastal Southern China in simulating heavy-rain-producing MCSs during the pre-summer rainy season. The other is to examine the influence of different time intervals and time spans of the radar DA on the forecasting of MCSs.

2. Case overview

This study investigates the MCSs that occurred in west coastal Guangdong and the nearby offshore areas on May 8, 2013, several days before the onset of the summer monsoon over the South China Sea. The control region in this study is an approximately 400 km×400 km square area centered on the Yangjiang S-band radar (Figure 1). To demonstrate the convection initiation and evolution, Figure 1a–j shows hourly time series of radar reflectivity at 3 km above sea level (ASL) derived from the Yangjiang radar during 0200–1100 Beijing Standard Time (BST; BST=UTC+8 h) on May 8, 2013, during which there were five MCSs in the observing area of the Yangjiang radar. One of those (MCS1) produced a large amount of rainfall in western Guangdong over a period of 7 h (0400–1100 BST), with heavy precipitation (>50 mm) extending from the southwest to the northeast, and a maximum amount of 284.7 mm (Figure 1k). The heavy rain-producing MCS1 was initiated near the city of Yangjiang at 0200 BST. It then intensified, extended toward northeast, and then moved eastward. At 0200 BST, there were two other MCSs, one in the southwest Guangdong coastal area (MCS2) and the other located further south over the sea (MCS3). Initiated at the junction of sea and land, MCS2 developed and strengthened until 0700 BST. It then moved eastward, comprising a few linear-shaped convective elements over the sea. Meanwhile, MCS3 moved eastward and disappeared from the control region at 0700 BST. At 0300 BST, MCS4 emerged to the north of MCS2, developed and propagated northeastward until 0500 BST, then started to weaken and disappeared around 1100 BST. At 0500 BST, a few new convective cells were initiated over the ocean. These grew and formed another MCS (MCS5) around 0700 BST. Afterward, MCS5 gathered, strengthened, and moved eastward. At 1100 BST, MCS1 over the land, MCS5 over the sea, and MCS2 offshore near the coast remained in the control region.

Figure 2 shows the major features of the synoptic background under which the heavy-rainfall event took place. The control region lay in front of a trough at 500 hPa, was dominated by southwesterly winds at 500 and 700 hPa, and was located in the convergence zone of the southwesterly and southeasterly winds in the South China coastal region at 850 and 925 hPa. The southeasterly winds in the planetary boundary layer (PBL) transported the high-θ_e air over the sea toward the control region (Figure 2d). The horizontal wind speeds from 925 to 700 hPa over South China and its adjacent waters were lower than 10 m s^{-1}, i.e., no strong low-level jets from the ocean were found. The precipitable water was 50–55 and 55–60 mm over the coastal South China and the offshore sea area, respectively (Figure 2a). Moreover, the convective available potential energy (CAPE) was 500–1000 J kg^{-1} around the control region (Figure 2c). The

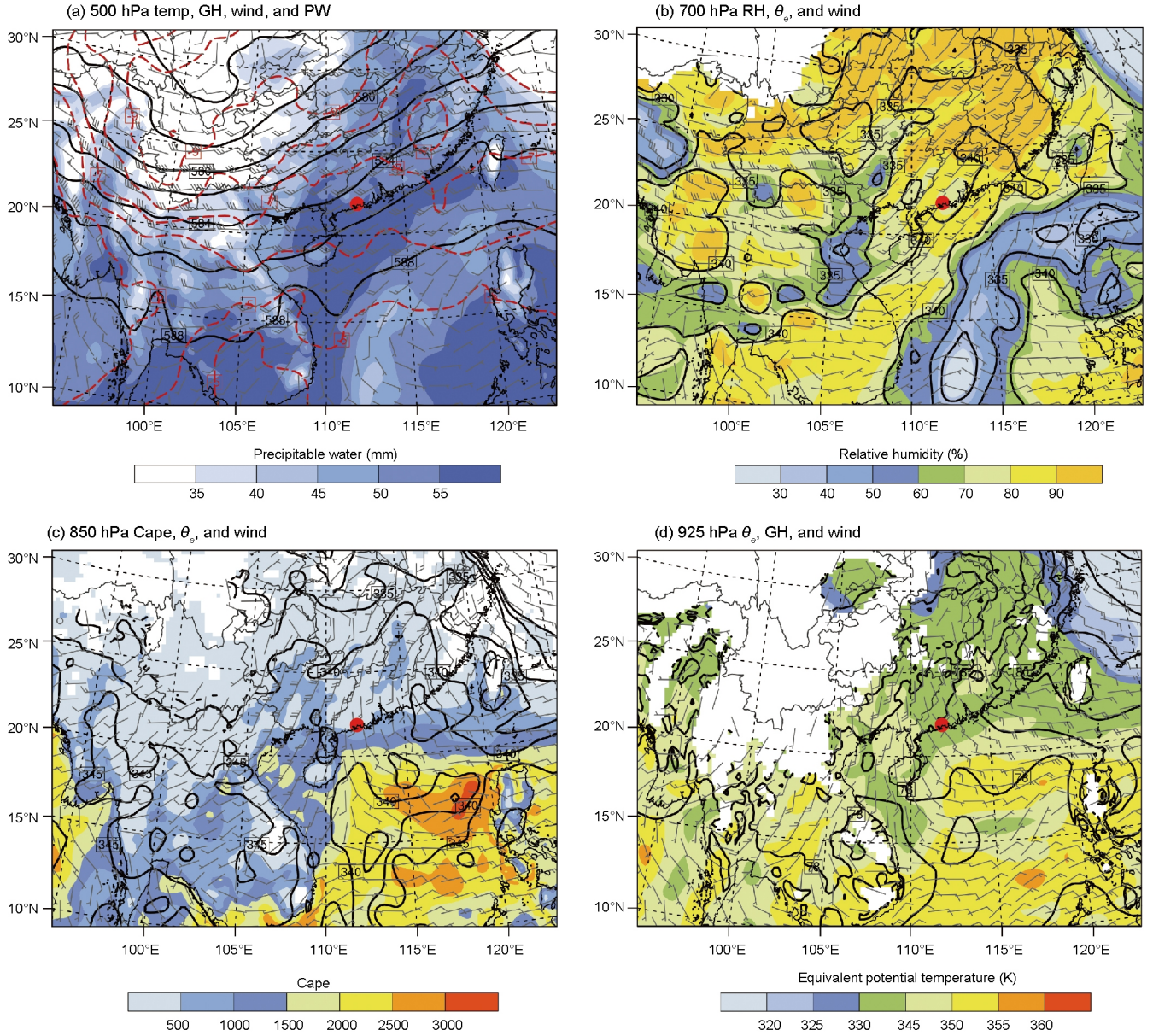

Figure 2 NCEP FNL analysis at 0200 BST 8 May 2013. (a) The 500-hPa geopotential height (solid contours at intervals of 20 m), temperature (dashed contours at intervals of 1°C), horizontal wind barbs, and precipitable water (mm, shaded). (b) The 700-hPa equivalent potential temperature (θ_e, contours at intervals of 5 K), relative humidity (%, shaded), and horizontal wind barbs. (c) The 850-hPa θ_e (contours at intervals of 5 K), horizontal wind barbs, and CAPE (J kg^{-1}, shaded). (d) The 925-hPa geopotential height (solid contours at intervals of 10 m),θ_e (K, shaded), and horizontal wind barbs. A full bar represents 5 m s^{-1}. The location of the Yangjiang radar is marked with a red dot in each panel.

aforementioned observations suggest that the atmospheric environment of the MCSs on May 8, 2013 was characterized by abundant moisture, moderate CAPE, and a lack of low-level jets. These environmental features are largely similar to those two days later when another localized extreme-rainfall event occurred over the Yangjiang area (Wang et al., 2014).

3. Methodology

3.1 The WRF-EnKF system

In the present study, 40 deterministic forecast experiments and 60-member ensemble experiments with radar DA are conducted using the WRF-based EnKF system that was originally developed for regional-scale DA at the Pennsylvania State University (Zhang et al., 2006b; Meng and Zhang, 2008a, 2008b; Zhang et al., 2009). Version 3.5.1 of the Advanced Research WRF (WRF-ARW) model (Skamarock et al., 2008) is employed in the present study. Four one-way-nested domains (D1-D4) are used with 43 vertical levels and a model top at 10 hPa. The domains consist of 166×166, 301×289, 529×508, and 916×664 grid points in the horizontal with grid spacings of 27, 9, 3, and 1 km, respectively (Figure 3). The initial and boundary conditions

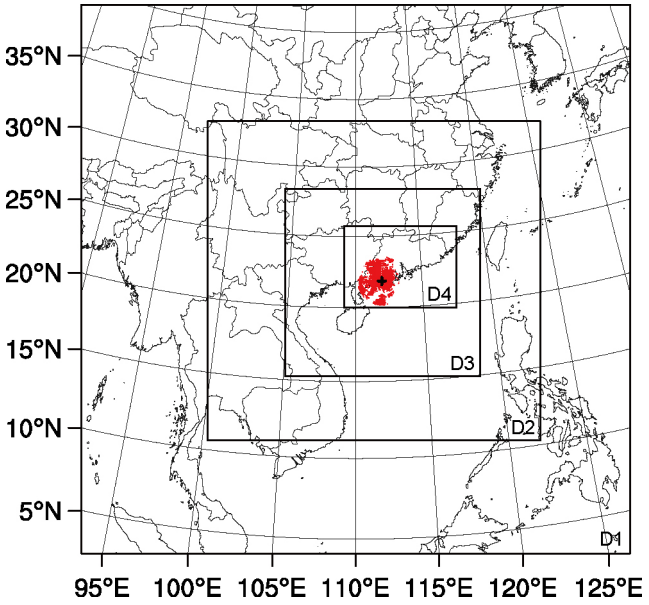

Figure 3 Model domain configuration. Location of Yangjiang radar is marked with a black cross. Red dots show the distribution of the super observations (SOs) at 0200 BST 8 May 2013.

are generated from the National Centers for Environmental Prediction (NCEP) final analyses (FNL) that are on 1°×1° grids and available every 6 h. The WRF single-moment (WSM) six-class microphysics (Hong et al., 2004), the YSU PBL scheme (Noh et al., 2003), and the thermal-diffusion land-surface scheme (Chen and Dudhia, 2001) are used for D1–D4. The Grell-Freitas ensemble cumulus scheme (Grell and Freitas, 2014) is turned on in D1 and D2, whereas no cumulus parameterization is used in D3 and D4.

For each DA experiment, the initial states of 60 members are generated by adding balanced perturbations to the NCEP/FNL analysis at 2000 BST 07 May 2013. The perturbations are generated using the "cv3" background error covariance option in the WRF 3DVar package (Barker et al., 2004). The perturbed variables include horizontal wind components, potential temperature, and mixing ratio for water vapor, and their standard deviations are approximated by the analysis errors of the FNL data, namely 2 m s^{-1} for wind, 1 K for temperature, and 0.5 g kg^{-1} for water-vapor mixing ratio. The lateral boundaries are produced using the same method. This ensemble initialization method has been used in previous studies (Meng and Zhang, 2008a, 2008b; Zhang et al., 2009; Luo and Chen, 2015; Zhu et al., 2016). The covariance relaxation method proposed by Zhang et al. (2004) (their eq. (5)) is used to inflate the background-error covariance with a relaxation coefficient of 0.8 (Zhang et al., 2009; Weng and Zhang, 2012; Zhu et al., 2016).

The DA is performed for the outer three domains (D1–D3). Following previous studies (Zhang et al., 2009; Weng and Zhang, 2012; Zhang and Weng, 2015; Zhu et al., 2016; Qiu and Zhang, 2016), the successive covariance localization (SCL) method (Zhang et al., 2009) is adopted to assimilate the radar observations. This method uses the fifth-order correlation function proposed by Gaspari and Cohn (1999) for covariance localization. A different horizontal-localization radius of influence (ROI) is used to acquire information about weather systems of different scales. In the present study, ROIs of 810, 270, and 90 km are used and 11%, 22%, and 67% of the data are assimilated in D1, D2, and D3, respectively, while the ROI in the vertical direction is set to the model depth (including all of the 43 vertical levels). The DA cycles of D1-D3 are performed sequentially. Namely, the DA cycle of each child domain is performed after completion of the DA cycle of its parent domain, using the parent-domain's ensemble boundary conditions.

3.2 Doppler-radar data processing

The radial velocities measured by the Yangjiang radar (e.g., Figure 3) are assimilated using the EnKF system in the DA experiments. The Yangjiang S-band Doppler radar is similar to the WSR-88D radars used in the United States (Zhu and Zhu, 2004). Detailed information about the features of this radar can be found in Wang et al. (2014). The automated Doppler-radar velocity dealiasing algorithm (Xiao et al., 2012) is used for velocity unfolding, whereupon the method of Zhang et al. (2009) is used for additional quality control and data thinning. For each angle, we obtain discrete data of 3-km resolution in the radial direction and 3° resolution in the azimuthal direction to produce a "super" observation (SO). The observation error of radial velocity is set to be 3 m s^{-1} for the assimilation. Distributions of SOs in the model domain at 0200 BST 7 May 2013 are shown in Figure 3. To show the real observations more clearly, the radar reflectivity and SO radial velocity from three scans (1.4°, 3.3°, and 6.0°) of the Yangjiang radar at 0400 BST 8 May 2013 are shown in Figure 4.

3.3 Experimental design

To investigate the influence of the DA time interval and span on the prediction of the MCSs, 40 DA deterministic forecast experiments (40 DADF) are conducted using the WRF-EnKF system with the DA time interval varying from 6–30 min and the DA time span from 0 to 2 h (Figure 5a). In each DADF experiment, the 60 members (D1–D3) are first integrated for 6 h to develop a high-resolution, flow-dependent background error covariance structure. The DA starts at the same time in each case (0200 BST 8 May 2013) but ends at different times between 0200–0400 BST, with a time interval of 6, 12, 24, and 30 min in the three domains D1–D3, respectively. Deterministic forecasts are initiated from the ensemble mean of the EnKF analyses right after the DA procedure is completed. Figure 5d gives the DA end time and the DA time interval of

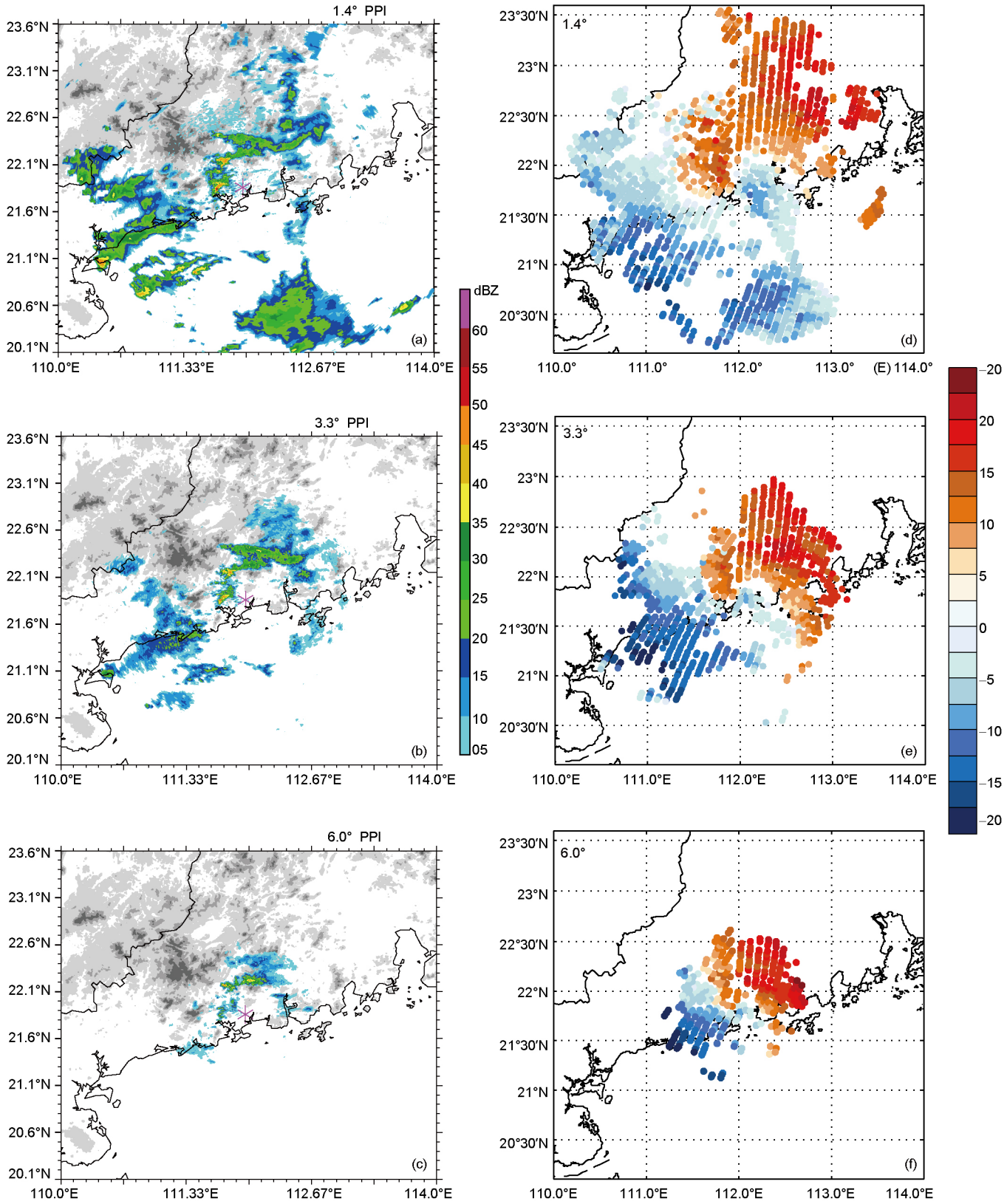

Figure 4 Radar reflectivity ((a)–(c)) and SO radial velocity ((d)–(f)) from the ((a), (d)) 1.4°, ((b), (e)) 3.3°, and ((c), (f)) 6.0° scans of the Yangjiang radar at 0400 BST 8 May 2013. Gray shading represents topography and gray lines denote the coastlines and provincial boundaries. The pink star in (a)–(c) denotes the location of the Yangjiang radar.

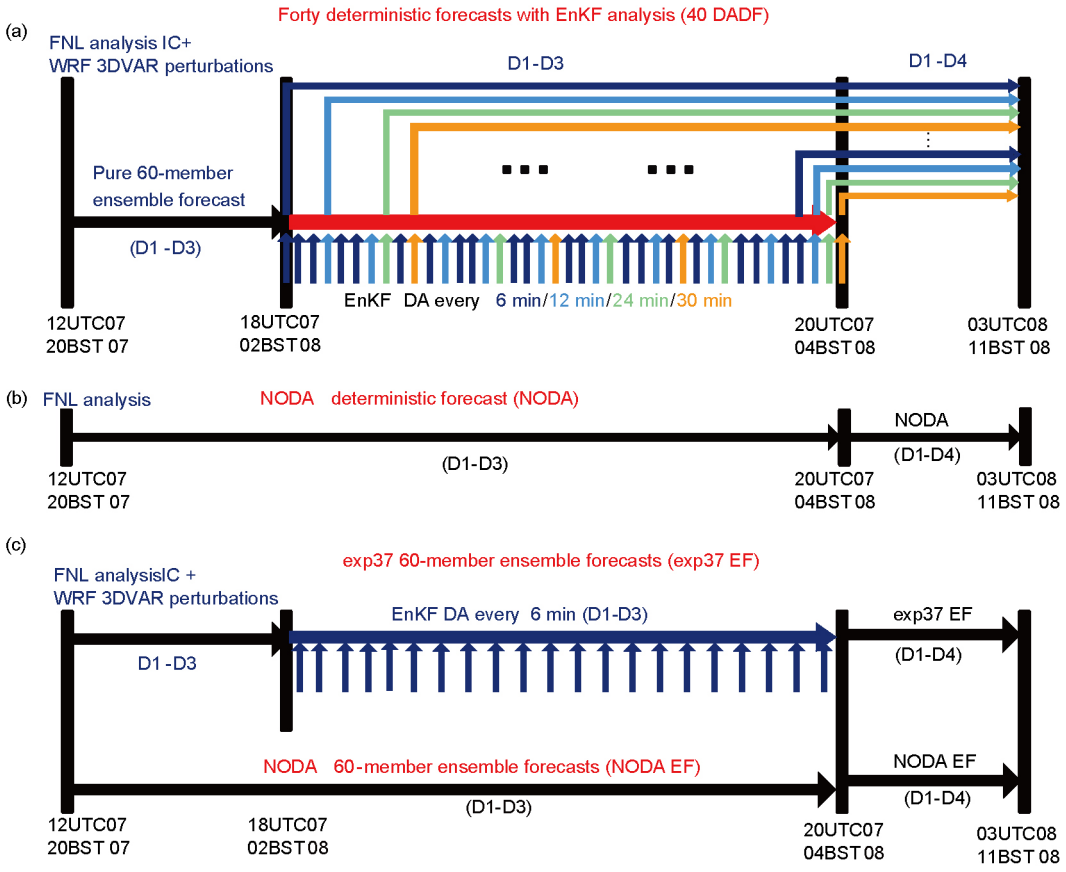

(d)

DA interval (min)																						
30						10					20					29					40	
24					8				16				24				32				39	
12			4		7		12		15		19		23		27		31		35		38	
06	1	2	3	5	6	9	11	13	14	17	18	21	22	25	26	28	30	33	34	36	37	
Experiments	18 00	18 06	18 12	18 18	18 24	18 30	18 36	18 42	18 48	18 54	19 00	19 06	19 12	19 18	19 24	19 30	19 36	19 42	19 48	19 54	20 00	
Ending time of DA																						

Figure 5 (a)–(c) Schematic flowcharts for (a) the 40 DADF experiment, (b) the NODA experiment, and (c) the exp37 EF and NODA EF experiments. Navy, blue, green, and orange thin arrows represent 6-min, 12-min, 24-min, and 30-min DA experiments, respectively. (d) List of the 40 DADF experiments. The numbers in color represent the experiment index. The DA time intervals (in min) are listed in the left column, while the DA end times (hh mm) are listed in the bottom row.

each DADF experiment. As a benchmark, an NODA experiment is performed using the WRF model as a deterministic forecast initiated from the NCEP FNL analyses at 2000 BST 7 May 2013 without the radar DA (Figure 5b). To analyze the impact of EnKF assimilation of radar observations on the probability forecast of the MCSs, the exp37 60-member ensemble forecast (exp37 EF) and NODA 60-member ensemble forecast (NODA EF) experiments are conducted (Figure 5c). The exp37 EF experiments are initiated from the 60 ensemble members of the EnKF analyses at the DA end time (0400 BST) of exp37 with 6-min time interval and 2-h time span. For comparison convenience, the NODA EF experiments are performed using the same perturbed ensemble members at 2000 BST 7 May 2013 as both the 40 DADF experiments and the exp37 EF experiments. Domain 4 (D4) is turned on at 0400 BST 8 May 2013 in all of these experiments. All experiments are integrated to 1100 BST 8 May 2013.

4. Convection prediction by NODA and the 40 DADF experiments

4.1 Convective evolution in NODA

Figure 6 shows radar reflectivity (dBZ) at 3 km ASL derived from NODA D4 during 0400–1100 BST 8 May 2013. Comparisons between Figure 6 and Figure 1c–j suggest that NODA largely captured the formation and morphology of MCS1 and MCS5 but missed the occurrences of MCS2, MCS3, and MCS4. Initiation and evolution of the simulated MCS1 and MCS5 still differ from the observations. The

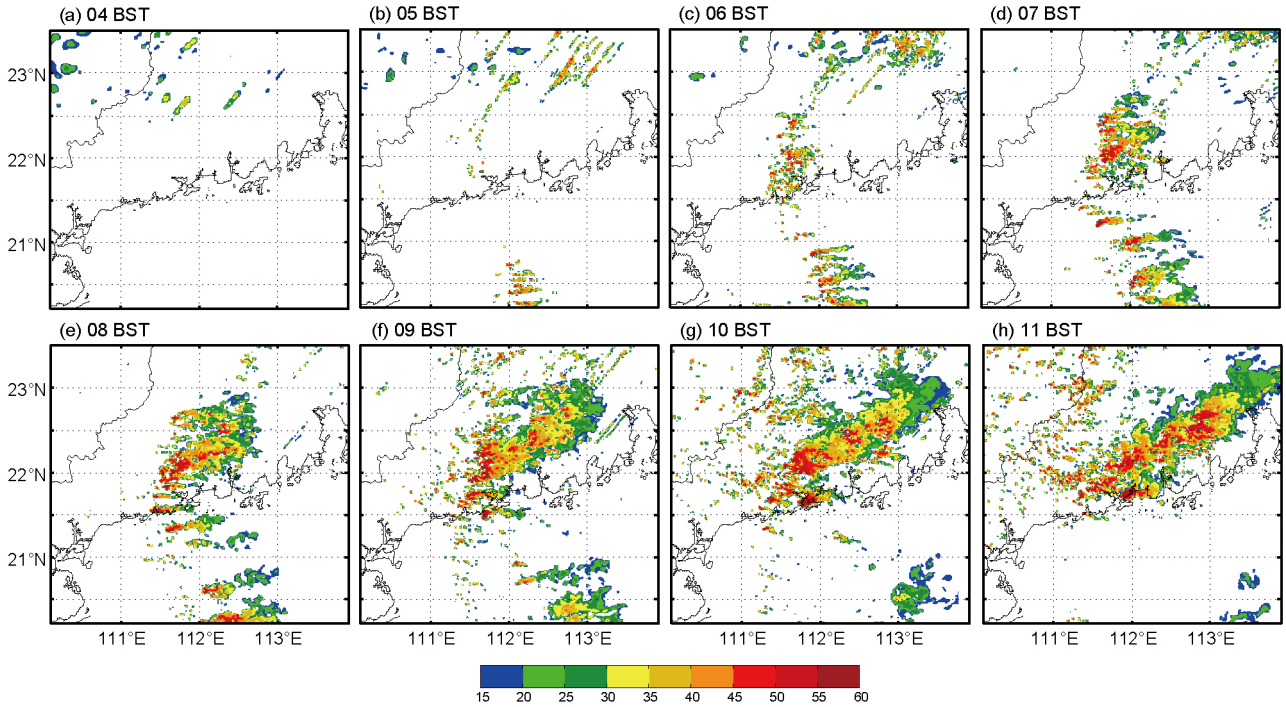

Figure 6 Radar reflectivity (dBZ) at 3 km ASL derived from NODA D4 during 0400–1100 BST 8 May 2013.

initiation of MCS1 at 0600 BST in NODA was 4 h later than that observed (at 0200 BST). The NODA-simulated MCS5 started to weaken at around 0900 BST and almost disappeared at 1100 BST, whereas the observed MCS5 maintained its strength until 1100 BST.

4.2 Convective evolution in the 40 DADF experiments

To evaluate the convective evolution in the 40 DADF experiments, a neighborhood ensemble probability (NEP) method (Schwartz et al., 2010) is used to verify the radar reflectivity forecasts. Similar to Snook et al. (2015), the radar observations are interpolated from the full radar reflectivity volumes to the model grid for the verification. A neighborhood radius of 2.5 km is used, resulting in a neighborhood consisting of 21 points in each member; thus, for the 40-member ensemble used, the ensemble-wide neighborhood consists of 840 forecast values.

Using the NEP method, the forecast probability of radar reflectivity exceeding 15 dBZ at 3 km ASL is calculated during 0400–1100 BST 8 May 2013, and compared with the corresponding reflectivity contours observed by the Yangjiang radar. These results are shown in Figure 7a–h. The areas with a high NEP of MCS1 closely match the regions where the observed reflectivity exceeds 15 dBZ throughout the forecast period, except that the high-NEP area is shifted slightly to the north of the observed MCS1 at 0600 BST and, at the late stage of the forecast (1000–1100 BST), the high-NEP areas corresponding to MCS1 move eastward more rapidly than does the observed MCS1. For MCS5, at the initial state (0500 and 0600 BST), there is a low-NEP area of large reflectivity to the south of the observed MCS5, suggesting that only several experiments simulated the initiation of MCS5 with some location errors. Shortly after, the NEP increases and the high-NEP area expands. Although the high-NEP area is still shifted somewhat to the south of the observed MCS5, the ensemble produces the evolution and movement of MCS5 with high probability during 0800–1100 BST.

The forecast probability of strong radar reflectivity (>30 dBZ) at 3 km ASL is also calculated using the NEP method. The results during 0800–1100 BST are shown in Figure 7i–l, while the results during the earlier hours are not shown because the MCSs are too weak, with very small areas exceeding 30 dBZ in both the observations and the ensemble experiments. The ensemble experiments overestimate the spatial coverage of large radar reflectivity (>30 dBZ) of MCS1. The NEP over land increases with forecast time. The high-NEP area over the land is slightly north of the observed MCS1 at 0800 BST and moves southeastward faster than does the observation. The high-NEP over the sea is located south of the observed MCS5, and moves eastward faster than does the observation, too. The NEP over the sea decreases after 0900 BST, indicating that fewer DADF experiments correctly predict the sustaining of MCS5 that is observed.

4.3 Comparison of AUC between NODA and the 40 DADF ensemble experiments

In this subsection, the performance of the NODA and 40

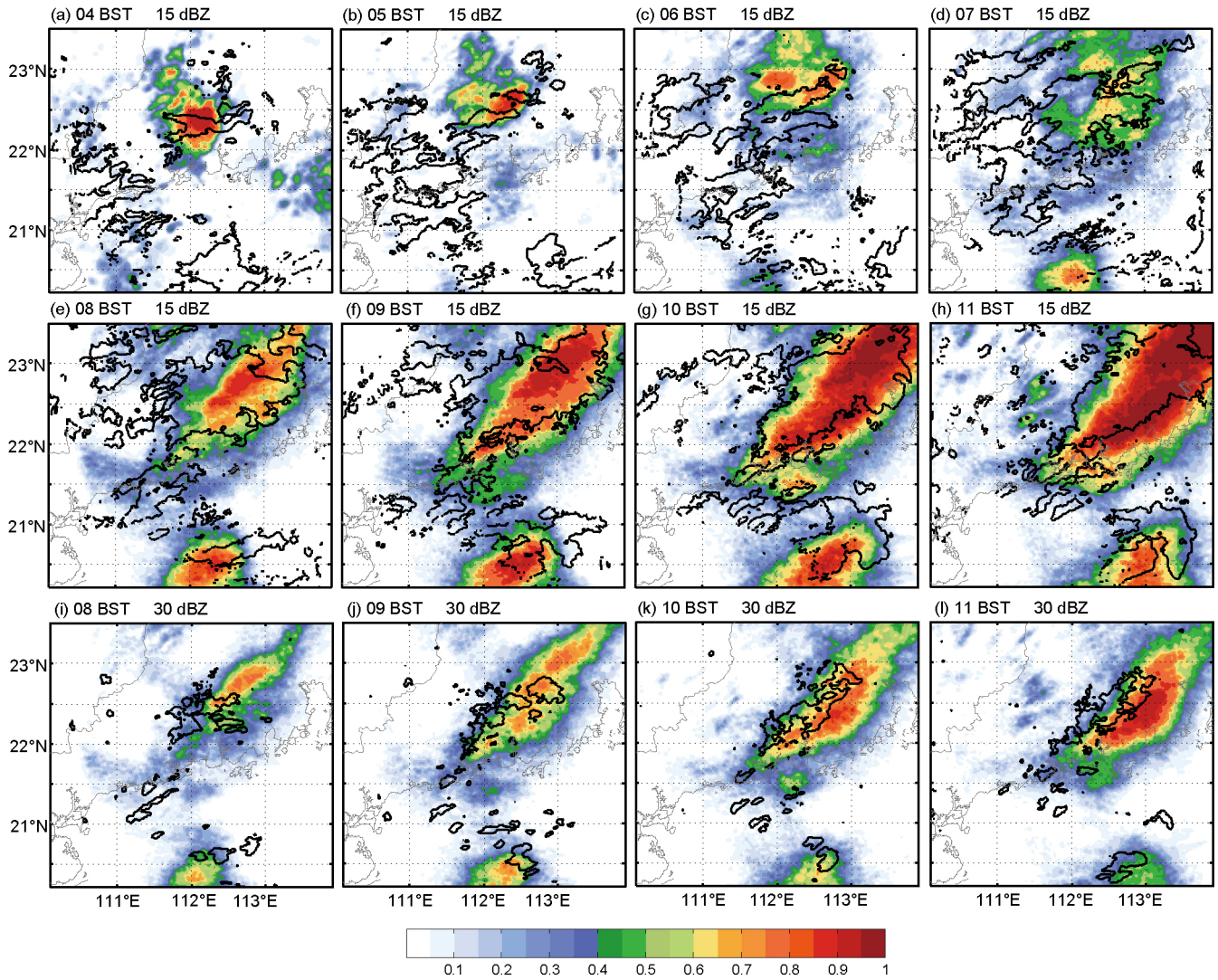

Figure 7 (a)–(h) Neighborhood ensemble probabilities (NEP; shaded) of the 40 DADF experiments that predicted radar reflectivity exceeding 15 dBZ at 3 km ASL during 0400–1100 BST. (i)–(l) As in (e)–(h), except for NEP of radar reflectivity exceeding 30 dBZ at 3 km ASL during 0800–1100 BST. The regions of radar reflectivity exceeding 15 and 30 dBZ in (a)–(h) and (i)–(l), respectively, observed by the Yangjiang radar at the corresponding times are outlined by bold black lines.

DADF experiments is compared using the area under the relative operating characteristic (ROC) curve (AUC; Mason and Graham, 1999, 2002) to examine the DA impact. The AUC has a maximum value of 1.0 for a perfect probabilistic forecast and a minimum value of zero. Scores at or below 0.5 indicate poor forecasts. Figure 8 shows the AUCs of the 40 DADF experiments and NODA for the radar reflectivity exceeding 15 dBZ at 3 km ASL over the control region. The AUC of NODA was less than 0.5 at 0400 and 0500 BST, suggesting that NODA is poor in the early stage. This is consistent with the feature of the simulated radar reflectivity at 3 km ASL, i.e., NODA does not correctly forecast the initiation and development of the MCSs. The AUC of NODA gradually increases with time after 0600 BST from 0.53 to 0.69 (Figure 8c–h), as NODA reasonably well simulates the development and shape feature of MCS1 during 0600–1100 BST (Figure 5). Although NODA already displays good forecasting ability after 0600 BST, more than half of the DADF experiments have a higher AUC compared to NODA during 0400–1100 BST except for 0600 and 0700 BST (Figure 8). These results confirm that assimilating the Yangjiang radar radial velocity using the EnKF method generally improves the simulation of convection initiation and evolution.

5. Influence of different DA time intervals and spans

Figure 8 shows that six maximal values of AUC during 0400–1100 BST belong to three experiments with 6-min time interval, i.e., exp28 (at 0800 and 0900 BST), exp36 (at 0400 and 0700 BST), and exp37 (at 0500 and 0600 BST), accounting for 75% of the eight times examined. Exp37 has

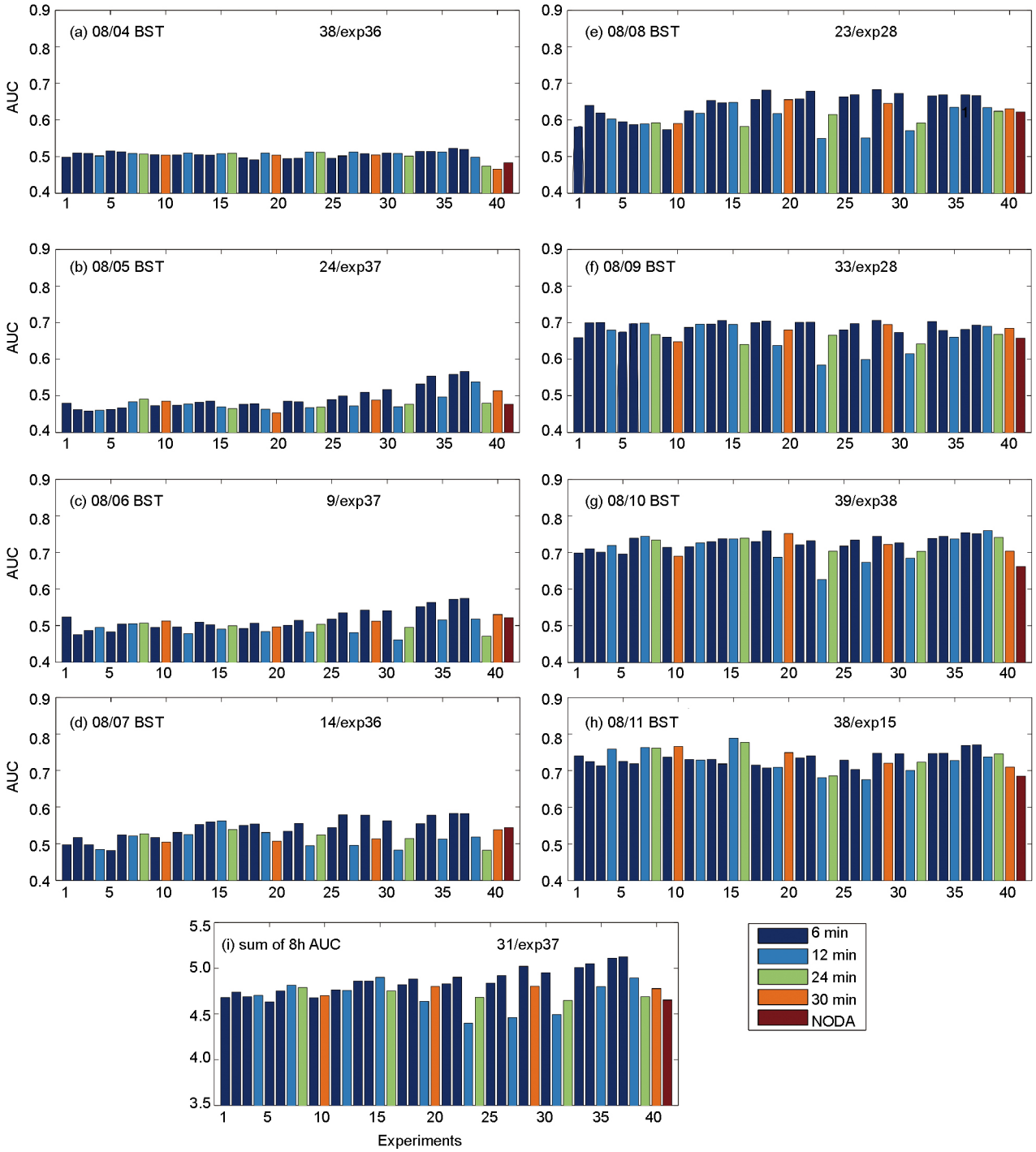

Figure 8 (a)–(h) Area under the ROC curve (AUC) of radar reflectivity at the 15-dBZ threshold at 3 km ASL from the 40 DADF experiments and NODA during 0400–1100 BST. (i) Sum of the 8-h (0400–1100 BST) AUC for radar reflectivity at the 15-dBZ threshold at 3 km ASL from the 40 DADF experiments and NODA. The numbers of DADF experiments with an AUC exceeding that of NODA and the experiment with the maximum AUC are labeled at the top right of each panel. The numbers 1–40 along the horizontal axis represent the 40 DADF experiments.

the largest AUC when summed over the eight evaluation times. The other two maximal values of AUC are obtained by exp15 and exp38, which use a 12-min DA time interval. However, the least skillful experiments (exp23, exp27, and exp31) also use 12-min DA time intervals, suggesting that a shorter time interval (i.e., 12 min) does not always help and could even result in degradation of the simulated convective evolution. Furthermore, the experiments with a 6-min DA time interval tend to have AUCs that increase with longer DA time span. This characteristic is hardly seen in the experiments with longer DA time intervals. For example, for the experiments with a 12-min time interval, the AUCs of

the experiments with longer DA time spans (exp23, exp27, and exp31) are even lower than those of the experiments with shorter time spans (e.g., exp4 and exp7) (Figure 8i). Nevertheless, exp37 with the shortest time interval and the longest DA time span has the highest AUC (Figure 8i).

To better understand these features, the root-mean-square errors of the radial velocity (RV RMSEs) for the EnKF forecast (ensemble mean field before DA) and the analysis (ensemble mean field after DA) are calculated. Almost all of the 6-min-interval experiments have the minimum RV RMSE of both the forecast and analysis, whereas the experiments with longer DA time interval do not have monotonic reduction of RV RMSE with shortening the DA time interval (not shown). Because the small errors of the initial state tend to grow rapidly and finally impact the forecast (Zhang et al., 2006a), it is unsurprising that the 6-min-interval experiments always show the best results and that the experiments with longer time intervals result in unstable forecasts.

We also calculate the hourly AUC of the 40 DADF experiments and NODA for radar reflectivity exceeding 30 dBZ at 3 km ASL during 0800–1100 BST and the sum of the four AUC values (Figure 9). NODA has an AUC of roughly 0.7, suggesting that the NODA experiment reasonably simulates the spatial distribution of convective cores with large radar reflectivity (>30 dBZ). Given this, it is not surprising that only 12 DADF simulations shows slightly better forecasting ability than that of NODA (Figure 9e). The majority of the 12 DADF experiments are those with a 6-min time interval. Similar to what has been found in the AUC results with a threshold of 15 dBZ (Figure 8), the lowest four values belong to experiments with a 12-min time interval (exp27, exp23, exp31, and exp19) (Figure 9e). In contrast to the AUC results using a threshold value of 15 dBZ, the experiment with highest AUC value is exp15 instead of exp37.

However, exp37 is identified as the optimal experiment for two reasons. Firstly, the AUC of exp37 for reflectivity greater than 30 dBZ is just slightly lower than that of exp15 (2.88 vs. 2.93), whereas the AUC of exp37 for reflectivity greater than 15 dBZ is much greater than that of exp15 (5.12 vs. 4.89). Secondly, the forecasting ability of the 6-min-interval experiments is more stable, showing fewer variations with different DA time spans compared with the experiments with a 12-min DA time interval. Therefore, in the following subsection, exp37 is compared with NODA and the observations to help understand the physical reasons contributing to the higher forecasting ability of exp37.

We reason that the group with a 6-min DA time interval show higher forecasting ability on the whole compared with

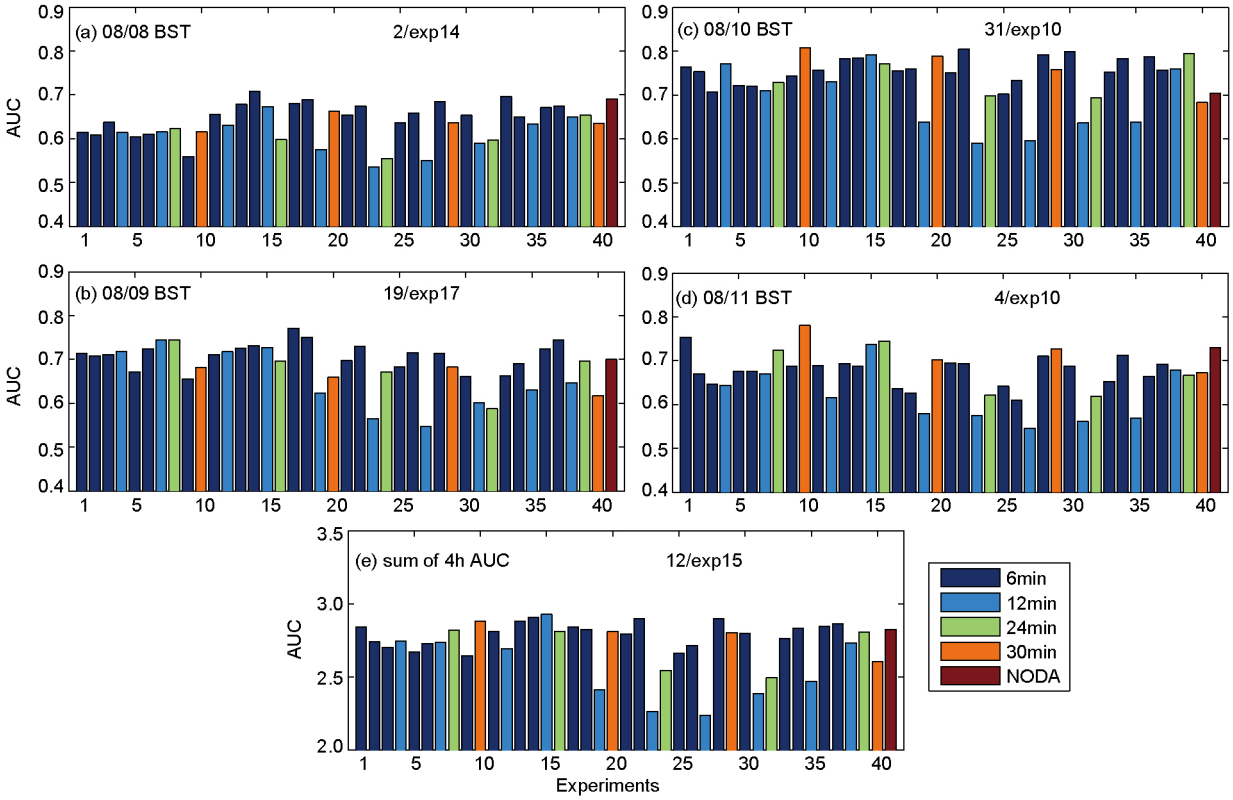

Figure 9 (a)–(d) Area under the ROC curve (AUC) of radar reflectivity at the 30-dBZ threshold at 3 km ASL from the 40 DADF experiments and NODA during 0800–1100 BST. (e) Sum of the 4–h (0800–1100 BST) AUC for radar reflectivity at the 30-dBZ threshold at 3 km ASL from the 40 DADF experiments and NODA. The numbers of DADF experiments with an AUC exceeding that of NODA and the experiment with the maximum AUC are labeled at the top right of each panel. The numbers 1–40 along the horizontal axis represent the 40 DADF experiments.

the other groups, and that the ability tends to improve with longer DA span, suggesting that assimilating more complete information of the radar velocity helps the convection prediction. In contrast, experiments using the longer time intervals (12, 24, and 30 min) result in less stable forecasts that do not tend to improve with longer DA span. The lower ability of some of those experiments could be attributed to the absence of important information contained in the radar radial-velocity observations that is not assimilated. Based on these results, we may state that, to better forecast the fast-evolving MCSs, it is safer to assimilate all observed radar velocity data with the shortest time interval (depending on the observation period of the equipment) and over as long a time span as possible.

6. Comparison between an optimal DADF experiment and NODA

This section compares an optimal DADF experiment (exp37) with NODA in relation to both their forecasts of convective evolution and their analysis fields. Figure 10 shows the radar reflectivity at 3 km ASL derived from the observation, NODA, and exp37 at four selected times. Compared with NODA, exp37 shows better simulations for MCS1, MCS4, and MCS5. The simulated radar reflectivity from exp37 at 0500 BST is close to the observation in relation to the presence and locations of MCS1, MCS2, MCS4, and MCS5 except for a larger extent and stronger intensity of MCS1, MCS4 and MCS5, whereas NODA produces only scattered convective cells over the sea that are similar to the observed MCS5 and misses the other MCSs at 0500 BST. The development of the major rain-producer in this case, namely MCS1, during 0700–1100 BST is captured well by both NODA and exp37, although its extent is smaller in NODA than it is in exp37. For MCS4, NODA essentially misses it whereas exp37 correctly simulates its location and its evolution from its powerful stage into its dying-out stage from 0500 BST to 0900 BST, despite some overestimation of its intensity. For MCS5, NODA suc-

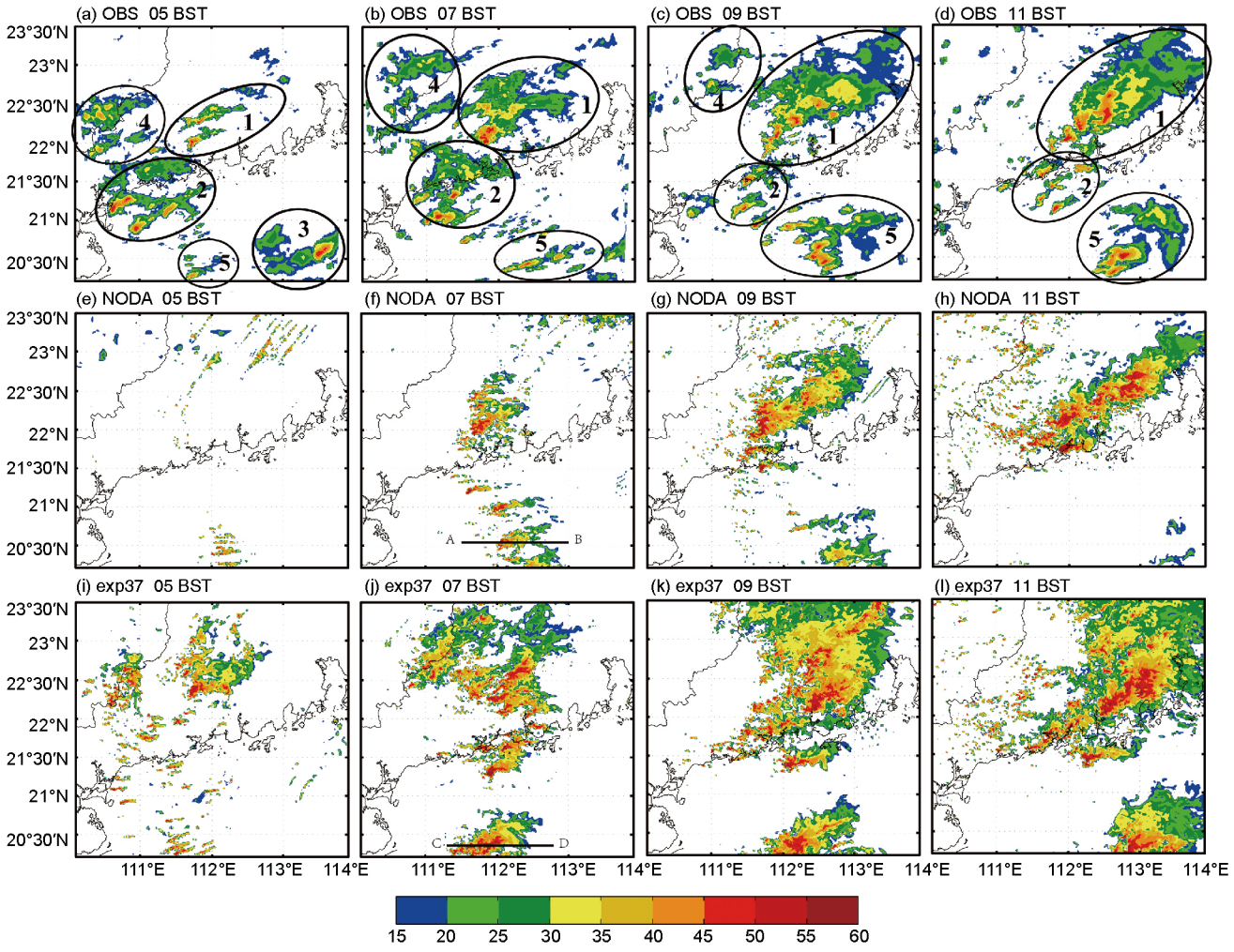

Figure 10 Radar reflectivity (dBZ) at 3 km ASL derived from the Yangjiang radar observations ((a)–(d)), NODA ((e)–(h)), and exp37 ((i)–(l)) at 0500, 0700, 0900, and 1100 BST. Ellipses 1–5 in (a)–(d) denote the regions of individual MCSs. The solid lines AB in (f) and CD in (j) represent the cross sections used in Figure 13a and 13b, respectively.

ceeds in simulating its initiation and intensification during 0500–0700 BST, but fails to simulate its maintenance: MCS5 weakens and disappears during 0800–1100 BST in NODA. In contrast, exp37 reproduces the maintenance of MCS5 until 1100 BST. These comparison results clearly demonstrate the better performance of exp37 over NODA for predicting MCS1, MCS4, and MCS5. However, neither NODA nor exp37 predict the development of MCS2 and MCS3.

Previous studies suggest that near-surface winds and underlying surface inhomogeneous features (topography and land/sea contrast) play important roles in convection initiation, as well as the fact that a surface mesoscale boundary that results from convective feedbacks (cold outflows) maintains heavy-rain-producing convective systems over the coastal areas of Guangdong in May (Wang et al., 2014; Wu and Luo, 2016). Therefore, wind and temperature fields on the first model level from NODA (Figure 11d–f) and exp37 (Figure 11g–i) at 0400 BST, 0700 BST, and 1100 BST are compared to the observations collected at the surface meteorological stations and automatic weather stations at the same times (Figure 11a–c). The regions of radar reflectivity exceeding 30 dBZ are outlined by blue contours in Figure 11a–i. To more clearly illustrate the difference between exp37 and NODA, the differences of the first-model-level temperature are shown in Figure 11j–l.

The surface observations show that southeasterly winds carry warm air over the sea toward the west-Guangdong coastal and offshore areas at 0400 BST (Figure 11a) supporting the development of the convective systems there (Figure 1c). After sunrise, the southeasterly inflows carrying warm (~27°C) and moist air are strengthened (cf. Figure 11a–c) and a mesoscale boundary between the warm airflow and the MCS1-generated cold outflows is formed at the southeast leading edge of the quasi-linear-shaped MCS1 (Figure 11c), supporting continuous convection initiation there and leading to maintenance of MCS1. The interaction of the southeastward vector (representing propagation of convective cells) and the northeastward vector (representing the environmental steering flow governing movement of convective cells) produces the eastward vector that represents the movement direction of MCS1 (Corfidi et al., 1996). That is, MCS1 moves eastward (Figure 1a–j) because of its interaction with the environmental steering flow (Figure 2a and b) and the contrast between the convectively generated cold outflow and the high-θ_e onshore inflow near the surface (Figure 11c).

At 0400 BST, both exp37 and NODA similarly produce a 2–3°C temperature contrast between the offshore (24–25°C) and land areas (~22°C) and a decrease in wind speed across the coastline (cf. Figure 11d and g). At 0700 BST and 1100 BST, although both NODA and exp37 simulate the southeasterly inflow feeding MCS1, the convectively generated cold outflow is much stronger in exp37 than it is in NODA (compare Figure 11e and h with Figure 11f and i) because of the earlier initiation and development of MCS1 in exp37. At 1100 BST, a mesoscale boundary is present in exp37 (Figure 11i) which is consistent with the observations, but it is not found in NODA (Figure 11f). A narrow band of negative temperature difference between exp37 and NODA over the leading edge of MCS1 (Figure 11l) reflects a stronger cold pool in exp37.

To better understand the improvements in exp37 relative to NODA (i.e., earlier initiation of MCS1 and longer maintenance of MCS5), Figure 12 shows the precipitable water (PW) and horizontal wind at 925 hPa from NODA and exp37 at the DA start time (0200 BST) and the DA end time (0400 BST) (Figure12a–d), as well as the corresponding difference of PW between exp37 and NODA (exp37 minus NODA) (Figure 12e–f) and the vertical profiles of the top 10% and the maximum vertical velocity (W) below 6 km in the environmental inflow area of MCS1 (green rectangles in Figure 12a–f) at the appropriate times (Figure 12g–h). At the DA start time, the PW differences range from −2 mm to 2 mm (Figure 12a, c, and e). When the DA is finished (0400 BST), the PW around the control region in exp37 becomes generally larger than that in NODA (0–2 mm). Moreover, the upward velocity of the environmental inflow in the low-middle layer has larger values in exp37 at both the DA start and end times. At 0200 BST, the max W (the top-10% W) in exp37 is 8–33 cm s^{-1} (1–13 cm s^{-1}) larger than that in NODA. At the lower levels (i.e., ~0.6 km), the max W in exp37 has a peak of roughly 52 cm s^{-1}, whereas the peak of max W is roughly 35 cm s^{-1} in NODA. At 0400 BST, the max W (the top-10% W) in exp37 is clearly larger than that in NODA as well. Between 0.2–2 km, the max-W value in exp37 is 32–37 cm s^{-1} whereas that in NODA is 24–32 cm s^{-1}. Therefore, compared with NODA, although the PW over the southeasterly inflow area in exp37 is only slightly more abundant (with a difference of 0–2 mm), the stronger upward motion in exp37 could lift the warm and moist inflow air to higher levels to trigger convection.

Around 0700 BST, MCS5 in NODA begins to weaken, whereas MCS5 in exp37 maintains its convective intensity. To better understand this difference in behavior, the vertical structures of MCS5 in NODA and exp37 at 0700 BST are compared (Figure 13). Specifically, Figure 13a and b shows the vertical cross sections of radar reflectivity, negative virtual-potential-temperature (θ_v) perturbation, and in-plane flow vectors through the MCS5 (along the black lines AB in Figure 10f (NODA) and CD in Figure 10j (exp37)) in NODA (exp37) at 0700 BST. The virtual-potential-temperature perturbation (θ_v') along the black line AB (the coordinates of points A and B are A (i_A, j_A) and B(i_B, j_A)) is defined by

$$\theta'_{v(i,j_A)} = \theta_{v(i,j_A)} - \frac{1}{5(i_B - i_A + 1)} \sum_{i=i_A,i_B} \sum_{j=j_A-2,j_A+2} \theta_{v(i,j)}. \quad (1)$$

In exp37, MCS5 is wide (~100 km across), deep (echo

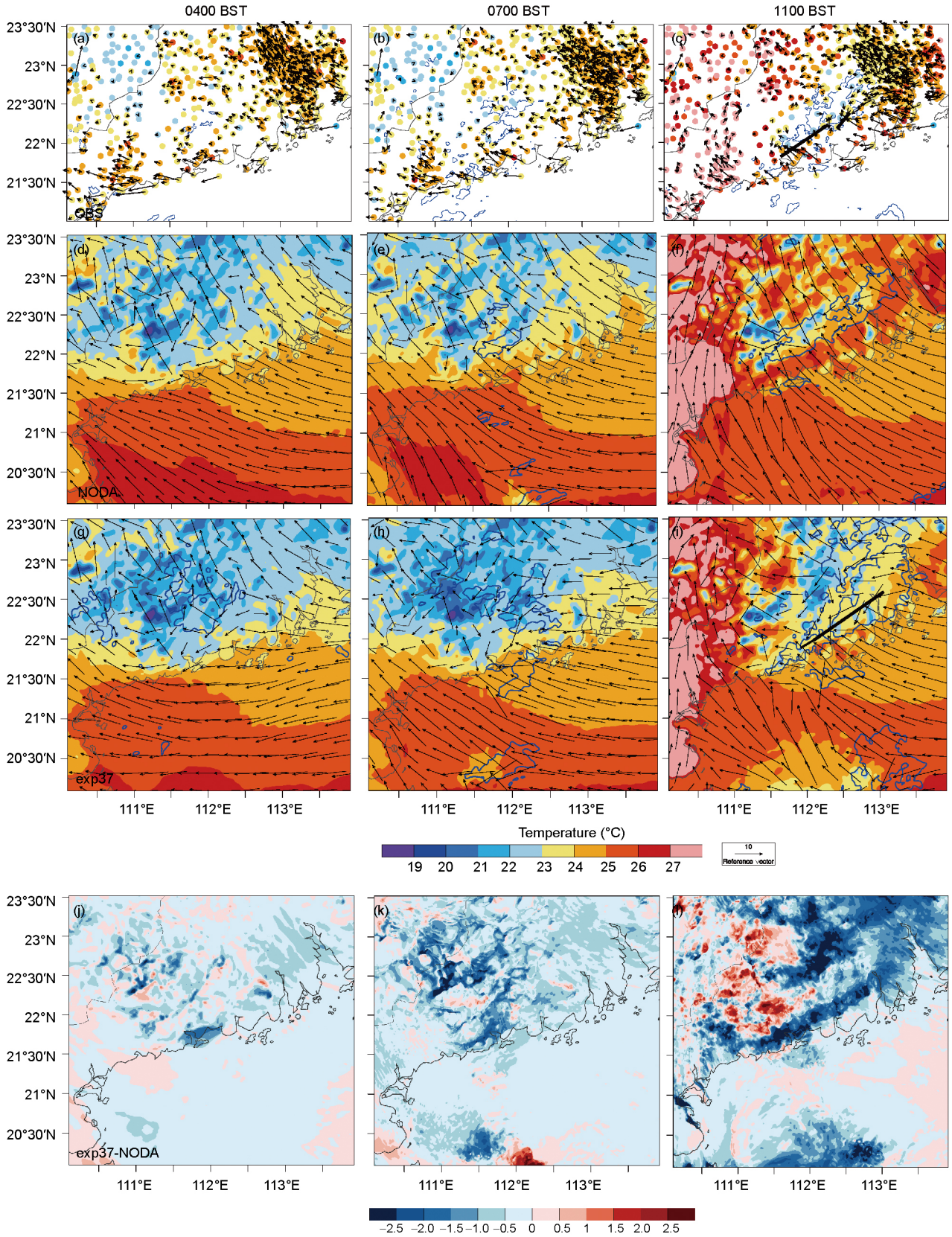

Figure 11 (a)–(c) Observed surface wind and temperature at 0400, 0700, and 1100 BST. Locations of surface AWSs are marked with dots, with colors representing the air temperature and black arrows representing the surface-wind vectors. Horizontal wind vectors and temperature (°C; shaded) at the first vertical level of (d)–(f) NODA and (g)–(i) exp37 at 0400, 0700, and 1100 BST, with the corresponding difference of the temperature between exp37 and NODA (exp37 minus NODA) are shown in (j)–(l). Corresponding regions of radar reflectivity exceeding 30 dBZ are outlined by blue contours.

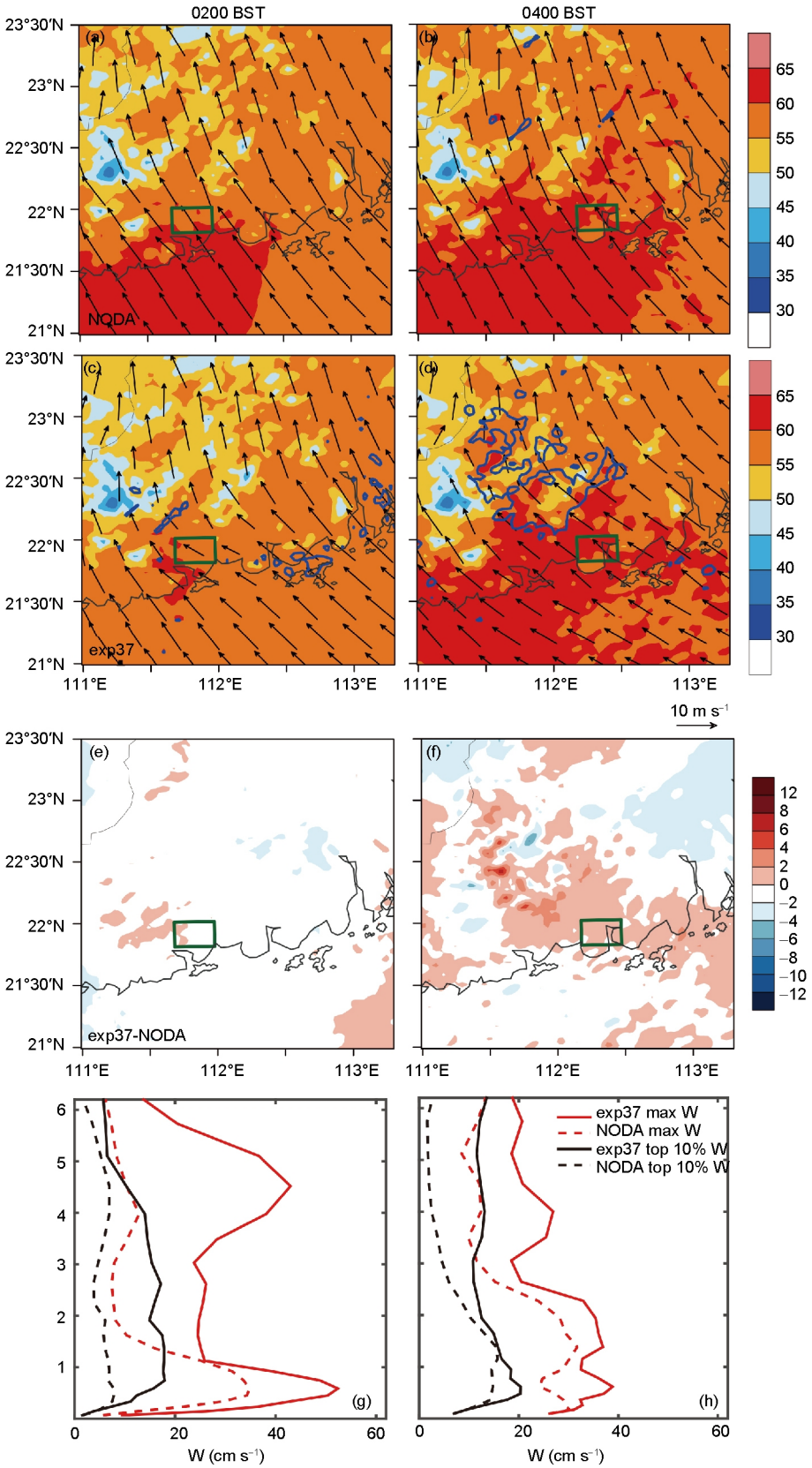

Figure 12 Precipitable water (PW; mm, shaded) and 925-hPa horizontal wind vectors from ((a), (b)) NODA and ((c), (d)) exp37 at 0200 and 0400 BST, along with ((e), (f)) the corresponding difference of PW between exp37 and NODA (exp37 minus NODA). Vertical profiles of the top 10% and the maximum vertical velocity (cm s^{-1}) below 6 km in the area that is indicated by the green rectangles in ((a), (c), (e)) at (g) 0200 BST and in ((b), (d), (f)) at (h) 0400 BST.

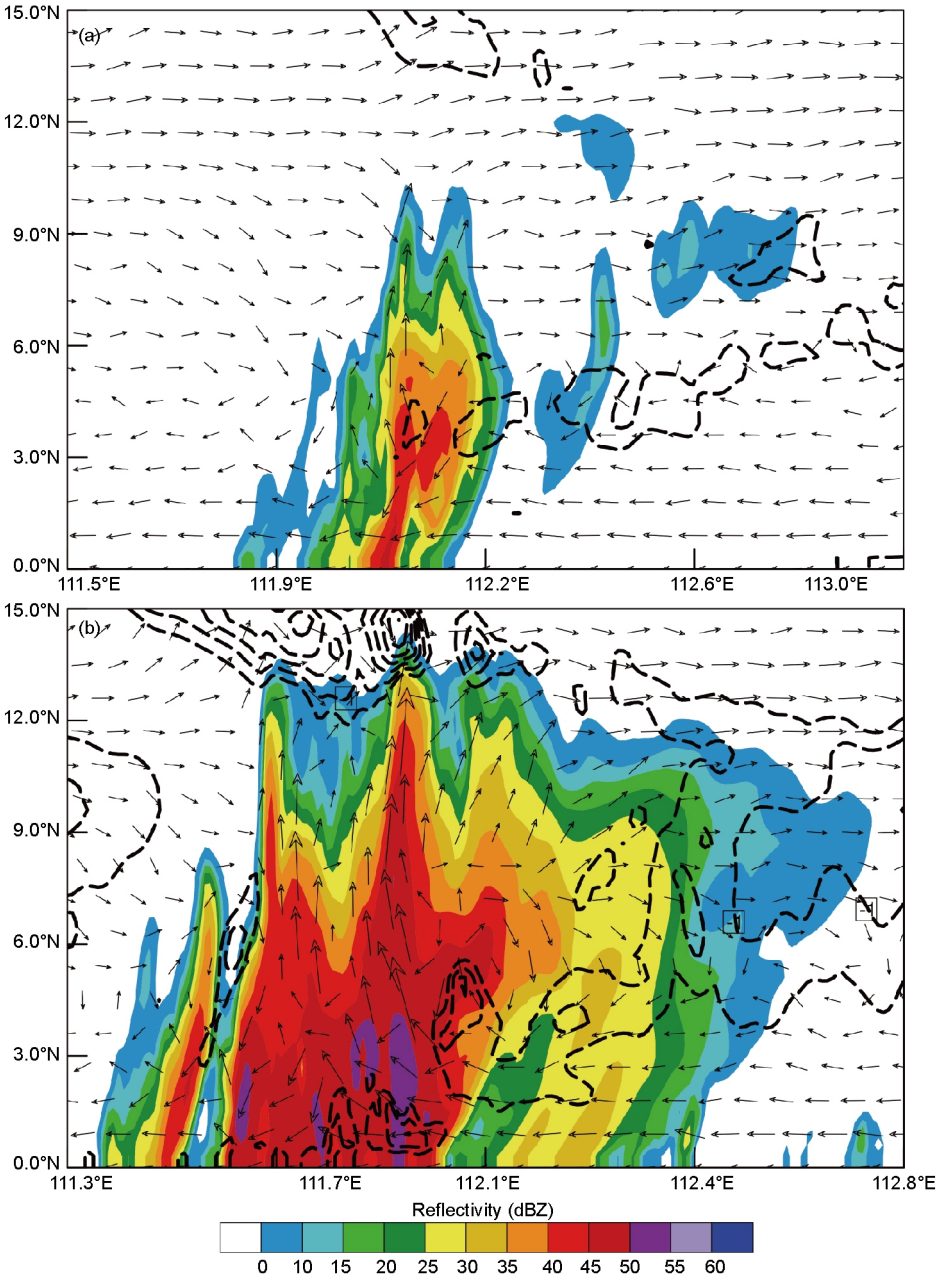

Figure 13 Vertical cross sections of radar reflectivity (dBZ, shaded), negative virtual-potential-temperature perturbation (dashed contours at 0.5-K intervals), and in-plane flow vectors along the line of the simulated MCS5 (i.e., AB and CD in Figure 10f and j) in (a) NODA and (b) exp37 at 0700 BST.

top extending up to ~14 km), and intense, with maximal reflectivity reaching 50–55 dBZ and updrafts extending up to 13 km (Figure 13b). Below 3 km ASL, there is a negative peak in θ_v' (<−1.5°C) located at the base of the maximum echo. At the top of this cold pool, the low-level inflow air is turning upward. This is similar to findings of Houze et al. (2009), who investigated continuous convective initiation in rain bands over the tropical ocean. They found that the cold pool generated by rain evaporative cooling at the base of the rain cell was strong enough to act as an impediment that raised the inflow air to its level of free convection and helped the convective initiation and maintenance. In contrast, at the same time in NODA (Figure 13a), MCS5 is significantly weaker in convective intensity, smaller in horizontal span, and shallower in vertical extension; for example, the updrafts with smaller magnitudes barely reach 9 km ASL. There is no cold pool at the base of the rain cell, while negative θ_v' values (<−0.5°C) are noticed in the middle layer (3–5 km). Consequently, the low-level inflow air hardly rises above its level of free convection, which contributes to rapid weakening of MCS5 in NODA.

In short, after assimilating the radar velocity data, the surface air on the land becomes moister and the rising velocity of the inflow air is greater in exp37. These are more favor-

able for the MCS1 initiation. In contrast, MCS5 at its earlier stage in exp37 is wider, deeper, and more intense than it is in NODA, leading to the production of a cold pool near the sea surface that lifts the unstable inflow air to the level of free convection and maintains MCS5 in exp37.

7. Influence of radar data assimilation on probabilistic forecasts

To investigate the impact of DA on probabilistic forecasts of the MCSs, we compare the NEP of radar reflectivity from the two sets of 60-member ensemble experiments, i.e., the NODA EF experiments and the exp37 EF experiments. As introduced in subsection 3.2, the two sets of ensemble experiments are initiated from the same 60-member perturbed ensemble initial fields at 2000 BST 7 May 2013; however, the DA is applied to the exp37 EF experiments every 6 min during 0200–0400 BST (Figure 5c). The NEPs of radar reflectivity exceeding 15 dBZ (30 dBZ) at 3 km ASL during 0400–1100 BST (0800–1100 BST) in the NODA EF experiments and the exp37 EF experiments are shown in Figures 14 and 15, respectively. For the 60-member ensemble used, the ensemble-wide neighborhood consists of 1260 forecast values.

The NEPs of radar reflectivity exceeding 15 dBZ from the NODA EF experiments at 0400 BST are close to zero in the analysis domain, except for a few scattered regions with low NEP (<0.3) located to the west of the observed MCS1 (Figure 14a), suggesting that most members fail to forecast MCSs at the initial state. Soon afterward, the NEP values near the observed MCS1 become higher with a larger area. However, the NEP values do not exceed 0.6 and the high-NEP area is still smaller than the observed MCS1 through the entire forecast period. For MCS5, there is a low-NEP region located to the south of the observed MCS5, and the NEP values are smaller than 0.4 during 0500–1100 BST (Figure 14b–h).

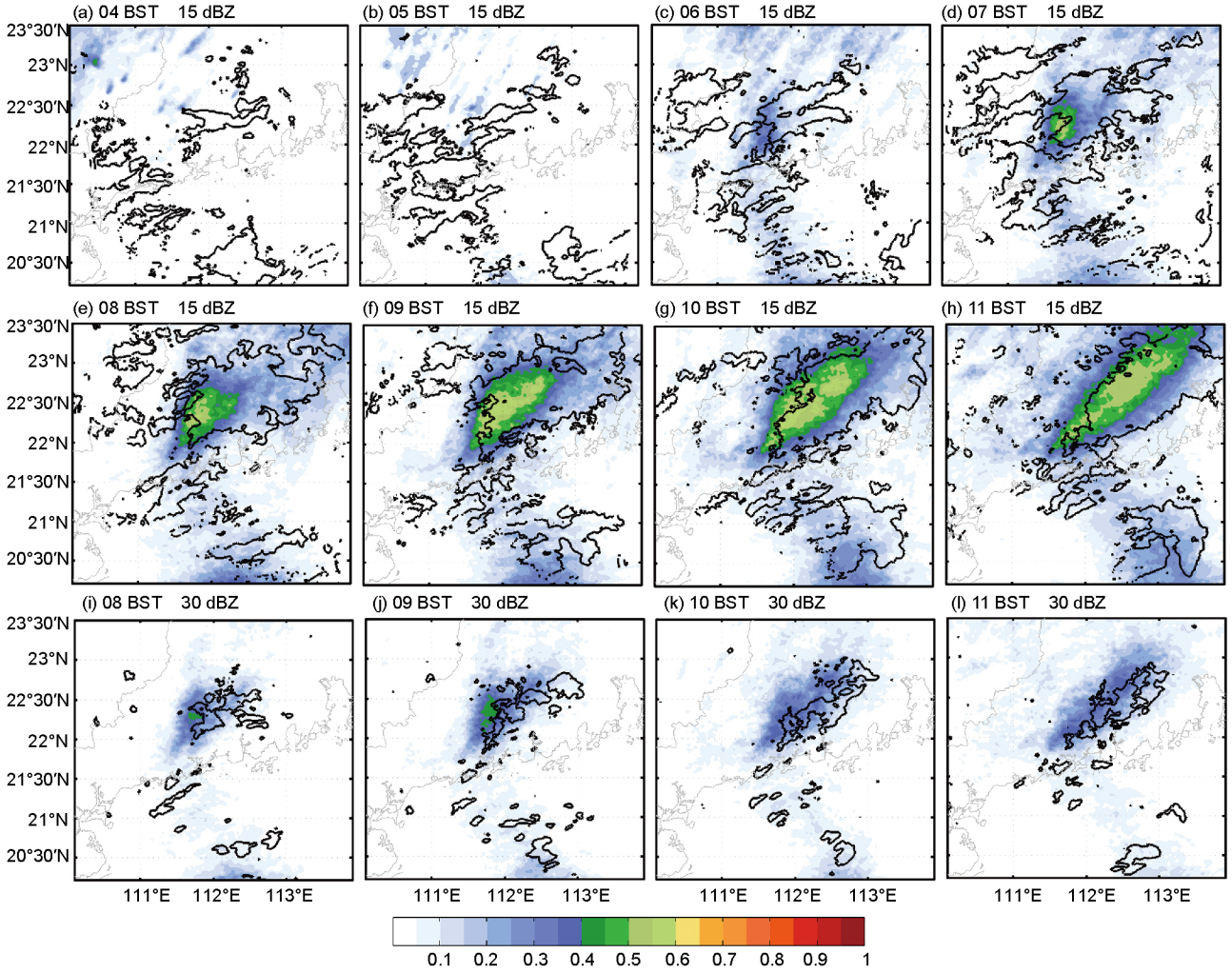

Figure 14 (a)–(h) Neighborhood ensemble probabilities (NEP; shaded) of the NODA EF experiments that predicted radar reflectivity exceeding 15 dBZ at 3 km ASL during 0400–1100 BST. (i)–(l) As in (e)–(h), except for NEP of radar reflectivity exceeding 30 dBZ at 3 km ASL during 0800–1100 BST. The regions of radar reflectivity exceeding 15 and 30 dBZ in (a)–(h) and (i)–(l), respectively, observed by the Yangjiang radar at the corresponding times are outlined by bold black lines. Gray lines represent the coastlines and provincial boundaries.

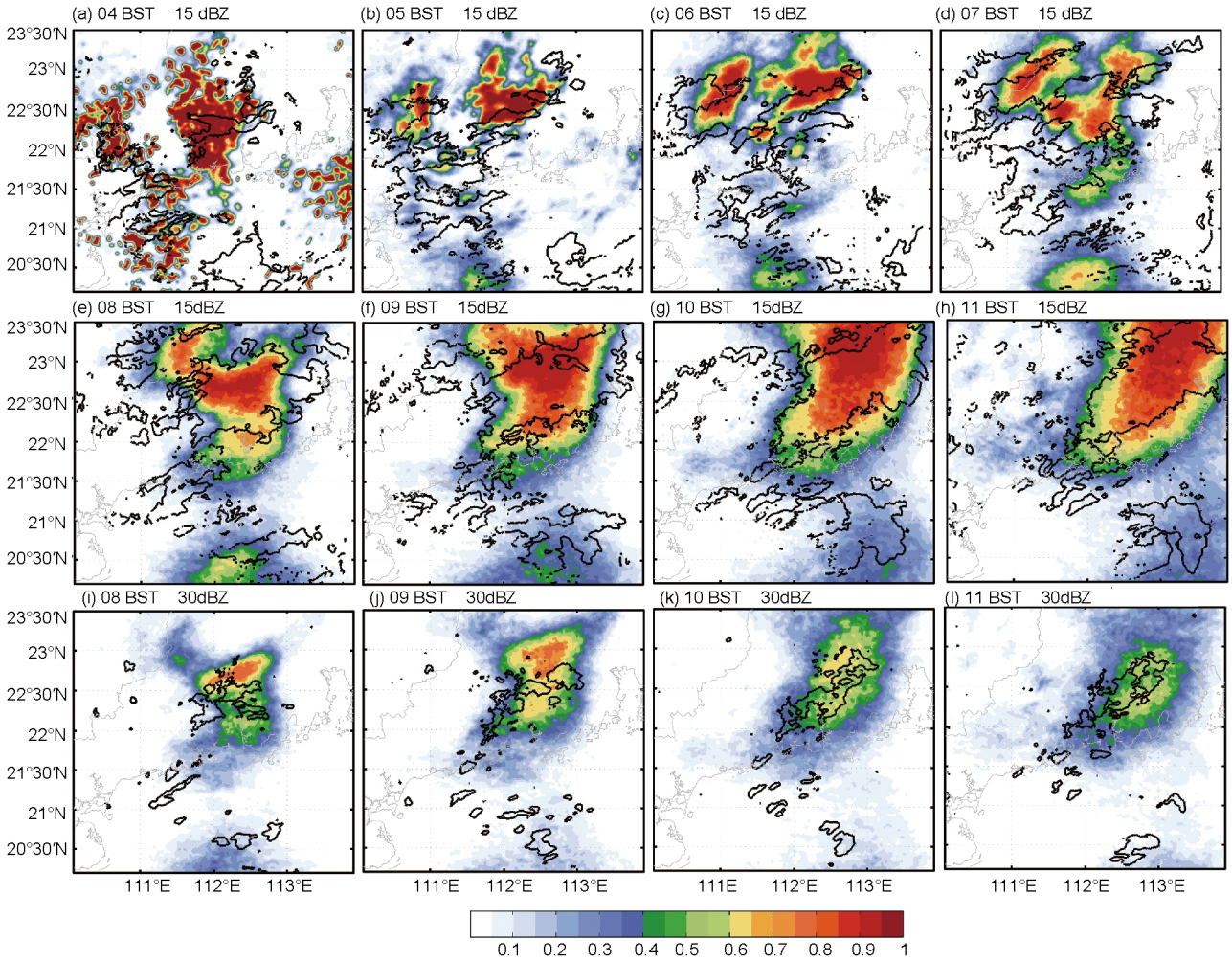

Figure 15 (a)–(h) Neighborhood ensemble probabilities (NEP; shaded) of the exp37 EF experiments that predicted radar reflectivity exceeding 15 dBZ at 3 km ASL during 0400–1100 BST. (i)–(l) As in (e)–(h), except for NEP of radar reflectivity exceeding 30 dBZ at 3 km ASL during 0800–1100 BST. The regions of radar reflectivity exceeding 15 and 30 dBZ in (a)–(h) and (i)–(l), respectively, observed by the Yangjiang radar at the corresponding times are outlined by bold black lines. Gray lines represent the coastlines and provincial boundaries.

Compared with the NODA EF experiments, the NEP of radar reflectivity exceeding 15 dBZ from the exp37 EF experiments is clearly more skillful for MCS1, MCS4, and MCS5 during the entire forecast period (Figure 15a–h). The NEP values are 0.8–1 in most of the high-NEP regions near MCS1 and MCS4. Although the high-NEP regions are wider than the observation at 0400 BST and with some displacement errors during 0500–0700 BST, the exp37 EF experiments reproduce MCS1 and MCS4 with high probability after the assimilation cycle. For MCS1, the high-NEP region closely matches the observation both in shape and extent during 0800–1100 BST. For MCS5, the exp37 EF experiments have higher NEP than those of the NODA EF experiments during 0500–1100 BST.

The NEP of strong radar reflectivity (>30 dBZ) at 3 km ASL during 0800–1100 BST is compared between the two ensemble experiments (Figures 14i–l, 15i–l). The NEP near MCS1 is substantially greater in the exp37 EF experiments (up to 0.8) than in the NODA EF experiments (<0.45), while the NEP value near MCS5 is also slightly larger. All these results suggest that the radar DA greatly improves the probability forecast of MCS1 over the land and MCS5 over the ocean.

8. Summary and conclusions

This work investigates the performance of a WRF-based EnKF in assimilating Doppler-radar radial-velocity data for convection-permitting prediction of MCSs over South China in the first heavy-rainfall event that occurred during the SCMREX 2013-IOP. Forty deterministic experiments with DA (40 DADF experiments) are generated using different time intervals and spans to assimilate the quality-controlled radial-velocity observations from the Yangjiang S-band radar. The initial ensemble (60 members) for the EnKF DA is generated by adding balanced perturbations to the FNL/NCEP analysis data at 2000 BST 7 May 2013, and integrated for 6 h to develop an approximately realistic,

flow-dependent background-error covariance structure before the first observation is assimilated. In the experiments, the DA starts at the same time (0200 BST 8 May) but lasts for different time spans (6 min to 2 h), with the time intervals used being 6, 12, 24, and 30min. Each deterministic forecast is initiated from the ensemble mean of the EnKF analyses. The reference experiment is conducted without DA (i.e., the NODA experiment) using the FNL/NCEP analysis at 2000 BST 7 May 2013 as the initial and lateral boundary conditions. To more clearly show the impact on the MCSs forecast by the radar DA, two sets of 60-member ensemble experiments (NODA EF and exp37 EF) are performed using the same 60-member perturbed ensemble initial fields at 2000 BST 7 May 2013, but with the radar DA being conducted every 6 min in the exp37 EF experiments from 0200–0400 BST. The major conclusions are as follows.

(1) The ensemble of 40 DADF experiments can predict the heavy-rain-producing MCSs over the land and another MCS over the ocean with high probability, despite slight displacement errors. The individual DADF experiments are generally better at convection prediction than is NODA. The exp37 EF greatly improves the probability forecast of the inland and offshore MCSs compared to the NODA EF. These findings support the effectiveness of DA and the advantage of convection-permitting ensemble forecasting for predicting convection development over the land and sea.

(2) Compared with the experiments using the longer DA time intervals, assimilating the radial-velocity observations at 6-min intervals tends to produce better forecasts. The experiment with the longest DA time span and shortest time interval shows the best performance. However, a shorter DA time interval (e.g., 12 min) or a longer DA time span does not always help, and could even result in degradation of the simulated convection evolution.

(3) Compared with NODA, the best-performing experiment with DA corrects errors in the simulated convective evolution in the inland, coastal, and offshore areas. By improving the representation of the initial state through the DA procedure, the dynamic and thermodynamic fields become more conducive for earlier initialization of the heavy-rain-producing MCSs in the inland area and longer maintenance of the MCS over the South China Sea.

Investigations of other heavy-rainfall cases during the SCMREX are ongoing, which is necessary for examining the generality of the findings obtained in the present study. Nevertheless, the encouraging results presented in this study demonstrate the great potential of assimilating Doppler-radar radial-velocity data in improving the forecasts of MCSs impacting the inland, costal, and offshore areas of South China during the pre-summer rainy season.

Acknowledgements *We are grateful to Prof. Fuqing Zhang (PSU) for his valuable comments. This study was jointly supported by the National Natural Science Foundation of China (Grant Nos. 41405050, 91437104 & 41461164006), the Public Welfare Scientific Research Projects in Meteorology (Grant No. GYHY201406013), and the National Basic Research Program of China (Grant No. 2014CB441402).*

References

Barker D M, Huang W, Guo Y R, Bourgeois A J, Xiao Q N. 2004. A three-dimensional variational data assimilation system for MM5: Implementation and initial results. Mon Weather Rev, 132: 897–914

Corfidi S F, Meritt J H, Fritsch J M. 1996. Predicting the movement of mesoscale convective complexes. Weather Forecast, 11: 41–46

Chen F, Dudhia J. 2001. Coupling an advanced land surface-hydrology model with the Penn State-NCAR MM5 modeling system. Part I: Model implementation and sensitivity. Mon Weather Rev, 129: 569–585

Ding Y H. 1992. Summer monsoon rainfalls in China. J Meteorol Soc Jpn, 70: 373–396

Ding Y H. 1994. Monsoons over China. Netherlands: Kluwer Academic Publishers. 419

Dong J, Xue M. 2013. Assimilation of radial velocity and reflectivity data from coastal WSR-88D radars using an ensemble Kalman filter for the analysis and forecast of landfalling hurricane *ike* (2008). Q J R Meteorol Soc, 139: 467–487

Evensen G. 1994. Sequential data assimilation with a nonlinear quasi-geostrophic model using Monte Carlo methods to forecast error statistics. J Geophys Res, 99: 10143

Gaspari G, Cohn S E. 1999. Construction of correlation functions in two and three dimensions. Q J R Meteorol Soc, 125: 723–757

Grell G A, Freitas S R. 2014. A scale and aerosol aware stochastic convective parameterization for weather and air quality modeling. Atmos Chem Phys, 14: 5233–5250

Hong S Y, Dudhia J, Chen S H. 2004. A revised approach to ice microphysical processes for the bulk parameterization of clouds and precipitation. Mon Weather Rev, 132: 103–120

Houze R A, Lee W C, Bell M M. 2009. Convective contribution to the genesis of Hurricane Ophelia (2005). Mon Weather Rev, 137: 2778–2800

Luo Y L, Wang H, Zhang R, Qian W, Luo Z. 2013. Comparison of rainfall characteristics and convective properties of monsoon precipitation systems over south China and the Yangtze and Huai River Basin. J Clim, 26: 110–132

Luo Y L, Chen Y R. 2015. Investigation of the predictability and physical mechanisms of an extreme-rainfall-producing mesoscale convective system along the Meiyu front in East China: An ensemble approach. J Geophys Res-Atmos, 120: 10,593–10,618

Luo Y L. 2017. Advances in understanding the early-summer heavy rainfall over South China. In: Chang C P, eds. The Global Monsoon System: III—A WMO Quadrennial Review. World Scientific Series on Asia-Pacific Weather and Climate, Vol. 9. World Scientific

Luo Y L, Zhang R H, Wan Q L, Wang B, Wong W K, Hu Z Q, Jou B J D, Lin Y L, Johnson R H, Chang C P, Zhu Y J, Zhang X B, Wang H, Xia R D, Ma J H, Zhang D L, Gao M, Zhang Y J, Liu X, Chen Y R X, Huang H J, Bao X H, Ruan Z, Cui Z H, Meng Z Y, Sun J H, Wu M W, Wang H Y, Peng X D, Qian W M, Zhao K, Xiao Y J. 2017. The southern China monsoon rainfall experiment (SCMREX). Bull Amer Meteorol Soc, 98: 999–1013

Mason S J, Graham N E. 1999. Conditional probabilities, relative operating characteristics, and relative operating levels. Weather Forecast, 14: 713–725

Mason S J, Graham N E. 2002. Areas beneath the relative operating characteristics (ROC) and relative operating levels (ROL) curves: Statistical significance and interpretation. Q J R Meteorol Soc, 128: 2145–2166

Meng Z Y, Zhang F Q. 2008a. Tests of an ensemble kalman filter for mesoscale and regional-scale data assimilation. Part III: Comparison with 3DVAR in a real-data case study. Mon Weather Rev, 136: 522–540

Meng Z Y, Zhang F Q. 2008b. Tests of an ensemble Kalman filter for

mesoscale and regional-scale data assimilation. Part IV: Comparison with 3DVAR in a month-long experiment. Mon Weather Rev, 136: 3671–3682

Noh Y, Cheon W G, Hong S Y, Raasch S. 2003. Improvement of the K-profile model for the planetary boundary layer based on large eddy simulation data. Bound-Layer Meteor, 107: 401–427

Qiu X X, Zhang F Q. 2016. Prediction and predictability of a catastrophic local extreme precipitation event through cloud-resolving ensemble analysis and forecasting with Doppler radar observations. Sci China Earth Sci, 59: 518–532

Schwartz C S, Kain J S, Weiss S J, Xue M, Bright D R, Kong F, Thomas K W, Levit J J, Coniglio M C, Wandishin M S. 2010. Toward improved convection-allowing ensembles: Model physics sensitivities and optimizing probabilistic guidance with small ensemble membership. Weather Forecast, 25: 263–280

Skamarock W C, Klpmp J B, Dudhia J, Gill D O, Barker D M, Duda M G, Huang X Y, Wang W, Powers J G. 2008. A description of the Advanced Research WRF version 3. NCAR Tech. Note NCAR/TN-4751STR, 113

Snook N, Xue M, Jung Y. 2011. Analysis of a tornadic mesoscale convective vortex based on ensemble Kalman filter assimilation of CASA X-Band and WSR-88D radar data. Mon Weather Rev, 139: 3446–3468

Snook N, Xue M, Jung Y. 2012. Ensemble probabilistic forecasts of a tornadic mesoscale convective system from ensemble Kalman filter analyses using WSR-88D and CASA radar data. Mon Weather Rev, 140: 2126–2146

Snook N, Xue M, Jung Y. 2015. Multiscale EnKF assimilation of radar and conventional observations and ensemble forecasting for a tornadic mesoscale convective system. Mon Weather Rev, 143: 1035–1057

Wang H, Luo Y L, Jou B J D. 2014. Initiation, maintenance, and properties of convection in an extreme rainfall event during SCMREX: Observational analysis. J Geophys Res-Atmos, 119: 13206–13232

Weng Y H, Zhang F Q. 2012. Assimilating airborne Doppler radar observations with an ensemble Kalman filter for convection-permitting hurricane initialization and prediction: Katrina (2005). Mon Weather Rev, 140: 841–859

Wu M W, Luo Y L. 2016. Mesoscale observational analysis of lifting mechanism of a warm-sector convective system producing the maximal daily precipitation in China mainland during pre-summer rainy season of 2015. J Meteorol Res, 30: 719–736

Xiao Y J, Wan Y F, Wang J, Wang B, Wang Z B. 2012. Study of an automated Doppler radar velocity dealiasing algorithm (in Chinese). Plateau Meteorol, 31: 1119–1128

Xu W X, Zipser E J, Liu C T. 2009. Rainfall characteristics and convective properties of Mei-Yu precipitation systems over south China, Taiwan, and the south China Sea. Part I: TRMM observations. Mon Weather Rev, 137: 4261–4275

Xue M, Dong J L. 2013. Assimilating best track minimum sea level pressure data together with doppler radar data using an ensemble Kalman filter for Hurricane Ike (2008) at a cloud-resolving resolution. Acta Meteorol Sin, 27: 379–399

Yue J, Meng Z Y. 2017. Impact of assimilating Taiwan's coastal radar radial velocity on forecasting Typhoon Morakot (2009) in southeastern China using a WRF-based EnKF. Sci China Earth Sci, 60: 315–327

Yue J, Meng Z Y, Yu C K, Cheng L W. 2017. Impact of coastal radar observability on the forecast of the track and rainfall of Typhoon Morakot (2009) using WRF-based ensemble Kalman filter data assimilation. Adv Atmos Sci, 34: 66–78

Zhang F Q, Snyder C, Sun J Z. 2004. Impacts of initial estimate and observation availability on convective-scale data assimilation with an ensemble Kalman filter. Mon Weather Rev, 132: 1238–1253

Zhang F Q, Odins A M, Nielsen-Gammon J W. 2006a. Mesoscale predictability of an extreme warm-season precipitation event. Weather Forecast, 21: 149–166

Zhang F Q, Meng Z Y, Aksoy A. 2006b. Tests of an ensemble Kalman filter for mesoscale and regional-scale data assimilation. Part I: Perfect model experiments. Mon Weather Rev, 134: 722–736

Zhang F Q, Weng Y H, Sippel J A, Meng Z Y, Bishop C H. 2009. Cloud-resolving hurricane initialization and prediction through assimilation of doppler radar observations with an ensemble Kalman filter. Mon Weather Rev, 137: 2105–2125

Zhang F Q, Weng Y H. 2015. Predicting hurricane intensity and associated hazards: A five-year real-time forecast experiment with assimilation of airborne Doppler radar observations. Bull Amer Meteorol Soc, 96: 25–33

Zhang X B, Luo Y L, Wan Q L, Ding W Y, Sun J X. 2016. Impact of assimilating wind profiling radar observations on convection-permitting quantitative precipitation forecasts during SCMREX. Weather Forecast, 31: 1271–1292

Zhu L, Wan Q L, Shen X Y, Meng Z Y, Zhang F Q, Weng Y H, Sippel J, Gao Y D, Zhang Y J, Yue J. 2016. Prediction and predictability of high-impact western pacific landfalling tropical cyclone Vicente (2012) through convection-permitting ensemble assimilation of Doppler radar velocity. Mon Weather Rev, 144: 21–43

Zhu X Y, Zhu J J. 2004. New generation weather radar network in China (in Chinese). Meteor Sci Technol, 32: 255–258